Article

Interplay between Habit Plane and Orientation Relationship in an Electron Backscatter Diffraction Analysis: Using the Example of η′-Al$_8$Fe$_3$ in η-Al$_5$Fe$_2$

Hanka Becker [1,*], Ralf Hielscher [2,*] and Andreas Leineweber [1,*]

1   Institute of Materials Science, TU Bergakademie Freiberg, 09599 Freiberg, Germany
2   Institute of Applied Analysis, TU Bergakademie Freiberg, 09599 Freiberg, Germany
*   Correspondence: hanka.becker@iww.tu-freiberg.de (H.B.); ralf.hielscher@math.tu-freiberg.de (R.H.);
    andreas.leineweber@iww.tu-freiberg.de (A.L.); Tel.: +49-3731-392647 (H.B.); +49-3731-392689 (R.H.);
    +49-3731-392622 (A.L.)

Abstract: The Al$_5$Fe$_2$ intermetallic rouses interest due to its rapid formation at the interface between iron/steel and aluminum by reactive interdiffusion. Only in the last few years have the differently ordered states of that intermetallic been elucidated (η′, η″, η‴ and η^m). In the present work, the microstructural characteristics of the plate-shaped η′-Al$_8$Fe$_3$ phase regions in a η‴/η-phase matrix were investigated, determining the habit planes from two-dimensional electron backscatter diffraction (EBSD) maps. Within an η grain, there are altogether four variants of η′ with four characteristically crystallographic equivalent habit planes with respect to η. These habit planes have been determined based on their traces measured for differently oriented η containing the η′ plates, applying different methods. One method in particular makes use of the connection between orientation relationship and habit planes. Using these methods, the habit planes were determined as $\{hkl\}_\eta$ and $\{hkl\}_{\eta'}$, both with $\{1\ 1.8\ 2.5\}_{\eta/\eta'}$. Thus, essential characteristics of the microstructure are provided for further analysis of the phase transformation of the η phase to the η′-Al$_8$Fe$_3$ phase.

Keywords: Al$_5$Fe$_2$; Al$_8$Fe$_3$; phase transformation; microstructure; variants; habit planes; orientation relationship; group theory; electron backscatter diffraction (EBSD); MTEX

1. Introduction

Intermetallic Al- and Fe-containing phases frequently develop by reactive interdiffusion in the contact areas of alloy systems consisting of initially Fe-rich and Al-rich regions. Technologically relevant examples are hot-dip aluminizing of iron or steel substrates to obtain protective Al-alloy coatings or substance-to-substance bond joining of high-strength steel or cast iron parts to light-weight Al-alloys [1–18]. Such material combinations are of high technological relevance and have found wide application, e.g., in the fields of traffic engineering, mechanical engineering or construction engineering [19,20]. Intermetallic layers formed upon hot-dip aluminizing of steel and during other types of Fe–Al reactive interactions consist mainly of binary Al–Fe phases, e.g., θ-Al$_{13}$Fe$_4$ ("Al$_3$Fe") [4–6,12,13,18], η-Al$_5$Fe$_2$ [4–9,12,13,18,21], ζ-Al$_2$Fe and FeAl [5,13], or multinary intermetallic phases in the presence of alloying elements [14,22,23]. Often, the η-Al$_5$Fe$_2$ intermetallic is reported to be the most rapidly growing phase by far, dominating the microstructure, at least in the absence of further alloying elements [2,4,6,8,11–13,16,18,21].

Until recently, η-Al$_5$Fe$_2$ was believed to be a single phase with the atomic structure forming a framework containing channels which are disorderedly occupied by Al atoms (see Figure 1a,b). Recently, however, it was discovered that several ordered phases develop at temperatures below approx. 350 °C, whereas at high-temperature, the disordered phase exists over a compositional range of approx. 2.5 at% [24–27] between 70.6 at% and 73.0 at% [24]. For that phase, the plain letter η is used [24,28–31]. In contrast to considerations

in earlier works, the channels in the η phase existing at elevated temperatures were shown to contain both Fe and Al atoms with a composition-dependent ratio [30]. The ordered low-temperature phases encountered from low to high Al content are η″ [30] (also described as η″-$Al_{7+x}Fe_3$ [31]), $η^m$ [28], η′-Al_8Fe_3 [24,29] and η‴ [30]. See Table 1 for crystallographic details. While the order formation in the channels of η″ and η‴ requires movement of atoms over only short distances, largely keeping chemical composition and keeping the orthorhombic lattice metric of the parent η phase, the formation of the η′-Al_8Fe_3 phase requires more rearrangement of atoms including reduction of the atomic density in the channels [30], see Table 1. This manifests in a monoclinic distortion of the crystal structure with a change of the β angle to 90.51° pertaining to the original orthorhombic cell and a decrease in the unit cell volume by 1.36% [24], likely associated with a minor compositional change in the matrix, within which the η′ phase forms.

The Al_5Fe_2 layers form by reactive interdiffusion as columnar grains [4,11,13,16,17,32] with a pronounced [001] texture in growth direction [4,11,13,17,32]. However, nothing is known yet about the detailed characteristics of the microstructure after a phase transformation from the disordered state of the η phase to the different ordered states. Formation of such ordered states upon cooling, however, including the diffusion phenomena apparently involved upon formation of the η′ phase, may lead to local misfits and associated stresses, which can cause failure in Al_5Fe_2 layers within the surface region of hot-dip aluminized steel or in joined assemblies. Hence, a profound knowledge of the microstructures developing in Al_5Fe_2 upon ordering is strived for.

In the present study, we investigate the characteristics of the microstructure of the η′-Al_8Fe_3 phase existing in a matrix consisting of the ordered η‴ phase but mainly showing the characteristics of the η phase. The focus is put on identification of the habit plane of η′-Al_8Fe_3 within the matrix based on electron backscatter diffraction (EBSD) data. Special care is taken to reliably distinguish between matrix and η′-Al_8Fe_3 and emerging orientation variants of the latter. Further, the habit plane of the plate-shape precipitates is determined by evaluating two-dimensional SEM/EBSD data applying different methods. A new procedure is worked out combining the information on the misorientation matrix–precipitate and the information on the interface trace to get accurate information about the orientation of the habit plane. As will be indicated, the data and computer scripts are made available.
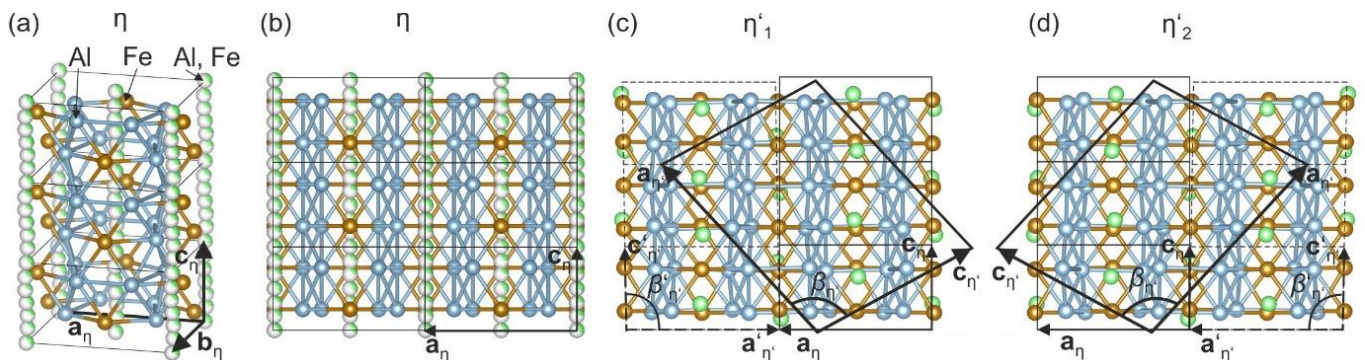
Figure 1. (**a**) Illustration of the crystal structure of the disordered, orthorhombic η-Al_5Fe_2 phase based on the structure model by Burkhardt et al. [33] modified by [30] with green atoms as the channel atoms (Al, Fe). Their partial occupancy is indicated by the degree of filling of the atomic spheres. Blue (Al) and orange (Fe) represent the atoms of the framework structure [30]. (**b**) View along the **b**-axis of the η-Al_5Fe_2 phase. (**c,d**) Analogous view of the two principal ways ($η′_1$ and $η′_2$) in which ordered η′-Al_8Fe_3 phase can be formed from η following the reduction of the symmetry of the crystal class from *mmm* to 2/*m* upon ordering (see Section 3.1). Additionally, the superstructure unit cell and the pseudo-orthorhombic subcell are indicated.

Table 1. Ordered and disordered phases of the Al_5Fe_2 field in the Al–Fe system. Whereas the disordered η' phase appears to exist over the range of 70.6 at% to 73.0 at% Al [30], the commensurately or incommensurately ordered phases appear to occur in narrower ranges of composition in the sequence as listed from low to high Al content (η'', η^m, η', η''').

Label	Formula	Order	Space Group	Approx. Number of Atoms Per Channel	Channel Atom Species	Reference
η	Al_5Fe_2	Disordered	*Cmcm*	1.47–1.5	Al and Fe	[24,31]
η''		Incommensurate [a]	*Xmcm(00g)0s0* *Immm(00g)0s0*	1.42–1.43	Al and Fe	[30]
	$Al_{7-x}Fe_3$	Commensurate	*Pmcn* [b]		Al and Fe	[31]
η^m		-	-	-	-	[28]
η'	Al_8Fe_3	Commensurate	*C2/c*	1.33	Al	[24,29]
η'''		Incommensurate [a]	$P2_1/c(0b0)00$ $P2_1/c(0b0)s0$	1.46–1.48	Al (Fe)	[30]

[a] The η'' and η''' phases were described as incommensurately modulated composite crystal structures, each composed of two composite subsystems. The first composite subsystem contains atoms of the framework's structure-generating channels which are filled by atoms described by the second composite subsystem. Each subsystem is described by an individual space group [30]. [b] Okamoto et al. [31] have described the η'' phase with several commensurate long-period superlattice structures differing by numbers of parent unit cells along the orthorhombic c-axis. All these superstructures were described using the same space group type.

2. Methods

2.1. Preparation and Heat Treatment of the Al-Fe Intermetallic Alloy

An induction-melted Al–Fe alloy produced from pure elements related to other studies [24,26,30] with 72.8 at% Al [24] was used in the investigation of the microstructure in the present study. The alloy was heat treated at 1000 °C for 120 h and at 750 °C for 48 h for homogenization. After subsequent milling in an agate mortar, the powder was heat treated at 250 °C for 624 h. During all heat treatments, the material was encapsulated in fused silica tubes under Ar atmosphere which were quenched in water after the heat treatments.

Powder X-ray diffraction analysis of the powder revealed simultaneous presence of the η' and the η''' phases [24]. While both phases exhibit characteristic superstructure or satellite reflections, the η' phase shows visible splitting of the fundamental reflections whereas the fundamental reflections of the η''' phase are unsplit and resemble those of the parent η phase. As the diffraction effects due to the respective superstructures plays no role in the present investigation, and to ease the discussion the pseudo-orthorhombic η''' phase is simply taken to as η. The corresponding lattice parameters are listed in Table 2. In the case of the η' phase, an η-like subcell (primed lattice basis vectors in Figure 1c,d) of the superstructure is used. In contrast to that of the η''' phase, however, this cell shows a visible monoclinic distortion, i.e., the β angle deviates from 90° by approx. 0.5°.

The part of the powder investigated here was embedded in epoxy resin and metallographically prepared to investigate the microstructure. The final preparation step of the cross section of the powder particles was polishing with OP-S suspension (Struers, Cleveland, OH, USA).

Table 2. Lattice parameters of the phases contained in the $Al_{72.8}Fe_{27.2}$ alloy powder investigated in the present work by EBSD analysis, as determined by Rietveld refinement from powder-XRD data of the same powder [24,30]. The unit cells chosen correspond to the orthorhombic cell of the parent disordered structure for simplicity (see also Figure 1). Atomic positions are given in Appendix A in Table A1. The respective primes for the lattice parameters emphasize that they refer to a subcell.

Phase	Subcell	Space Group	Lattice Parameters				Reference
			[Å]	[Å]	[Å]	[°]	
η''' (η)	Orthorhombic	*Cmcm*	a_η 7.6596	b_η 6.4070	c_η 4.2344	β_η 90	[30]
η'	Monoclinic/Pseudo-orthorhombic	$C2/c$ [a]	$a'_{\eta'}$ 7.6661	$b'_{\eta'}$ 6.4244	$c'_{\eta'}$ 4.1625	$\beta'_{\eta'}$ 90.494	[24] [b]

[a] The same space group symbol applies for the presently used subcell and for the actual superstructure (see Table 1). [b] Values related to the condition of the material that has been heat treated at 250 °C are not explicitly listed there.

2.2. Acquisition of EBSD Patterns

Microstructural investigations from the embedded powder particles by scanning electron microscopy were carried out employing a FEG Zeiss LEO 1530 GEMINI (Oberkochen, Germany) equipped with a Nordlys II EBSD detector (Oxford Instruments, Abingdon, UK) and HKL Channel5 software (Oxford instruments). EBSD pattern acquisition was performed at 20 kV in high-current mode with an aperture of 120 μm. EBSD patterns were recorded with 5 ms per frame and 5 frames to achieve a compromise between pattern quality, scan speed and drift. The EBSD patterns with a size of 336 × 256 pixels (4 × 4 binning) were stored for subsequent analysis with different indexing parameters. Altogether 23 particles were investigated by collecting EBSD maps while tilting the specimen by 70°. From all these particles, complementary backscatter electron images were taken in the untilted state.

2.3. Indexing of EBSD Patterns

Indexing was carried out by a Hough-space related indexing method. Keeping the used part of the EBSD patterns constant, the Hough-space resolution was set to the software specific maximum value of 125 [34] to consider the maximum possible accuracy during detection of the experimental band positions. Using this procedure, 8 Kikuchi-band positions were detected per EBSD pattern by analyzing the Kikuchi-band edges.

For indexing, special care was taken to apply properly chosen lattice parameters for phase indexing and pattern center calibration. Hence, the precise lattice parameters from powder-XRD analysis of the same powder as listed in Table 2 were employed. Atomic positions as established in the disordered crystal structure model of the disordered η-Al_5Fe_2 by Burkhardt [33] were used for both phases to obtain similar structure factors for the reflectors of both phases. This is justified because the employed Hough-space indexing method mainly uses positions of bands with high intensity and, thus, is restricted by only using the metric differences to distinguish the phases, while ignoring possible bands due to the superstructures. Intensity is only considered by the order of the reflectors. Thus, lattice plane families of relative kinematic intensity from 100% to 16% are used including 38 reflectors.

The positions of a minimum of 7 of 8 detected bands matching the simulation were required for indexing. Typically, several similar indexing solutions were obtained, of which that with the smallest mean angular deviation (MAD) was taken as best solution, and accepted for further evaluations.

The correctness of the calibration of the EBSD patterns was evaluated in detail (see Section 4.2). Most patterns were indexed several times by systematically varying the calibration parameters of the projection center in X (PCX) and in Y (PCY) coordinates to achieve reasonably good indexing results in qualitative terms. Furthermore, variation of

the vertical to horizontal ratio (V/H) and the detector distance (DD) was investigated and found to have only a minor effect on the indexing results (not shown).

2.4. Data Analysis

Data analysis was performed based on MATLAB (Natick, MA, USA) including the MATLAB toolbox MTEX [35,36]. The MTEX scripts used to determine the habit planes and generate the Figures 7, 8 and A3 are freely available at https://github.com/mtex-toolbox/mtex-paper/tree/master/EtaHabitPlane (accessed on 7 May 2022).

3. Theory

3.1. Crystallographic Characteristics of η′ Variants in η

Many phase transformations involve *partial* transformation of a *parent* phase towards a *child* phase which ends up embedded within the parent phase matrix. Typically, there is an orientation relationship (OR) between the crystal structures of the parent and the child phases. A typical case, relevant here, is high symmetry in the parent and a lower symmetry for the child phase, where the space groups are in a group–subgroup relationship [37–39]. Whereas loss of translational symmetry leads to antiphase domains, loss of point group symmetry leads to orientational variants, the latter being considered in the present work. This limits discussion of the symmetry to the level of point group, denoted with $\mathcal{G}^{\mathrm{P}}$ and $\mathcal{G}^{\mathrm{C}}$, the crystallographic point groups (crystal classes) of the parent and child phases, respectively.

It has been argued that the ratio of the orders of these point groups of the crystal structures, expressed as $|\mathcal{G}^{\mathrm{P}}|/|\mathcal{G}^{\mathrm{C}}|$, yields the number for orientational variants [37,39]. However, as pointed out in [38], upon reviewing different branches of scientific literature on the crystallography of phase transformations, this is only true if the OR implies spatial coincidence of the symmetry elements inherited by the child crystal from the parent crystal. Instead, what matters for calculation of the number of orientation variants is the *intersection group* $\mathcal{H}$ [40], which is a point group containing those symmetry operations which are spatially in coincidence for parent and child phase in view of their actual orientation relationship. Thus, the number of orientational variants is given by $|\mathcal{G}^{\mathrm{P}}|/|\mathcal{H}|$. Consequently, it was *not* considered a prerequisite that $\mathcal{G}^{\mathrm{C}}$ is a subgroup of $\mathcal{G}^{\mathrm{P}}$, which is relevant for many precipitation or martensitic transformations and for many transformations labeled "reconstructive" [41]. It is noted, however, that this does not exclude validity of the approach for cases where $\mathcal{G}^{\mathrm{C}}$ is indeed a subgroup of $\mathcal{G}^{\mathrm{P}}$.

In the current case, the point groups are $\mathcal{G}^{\mathrm{P}} = mmm$ (group order $|\mathcal{G}^{\mathrm{P}}| = 8$) for the parent η phase and $\mathcal{G}^{\mathrm{C}} = 1\,2/m\,1$ (group order $|\mathcal{G}^{\mathrm{C}}| = 4$) for the child η′ phase, fulfilling a group–subgroup relationship. Hence, in the sense of [37,39], the group order ratio amounts to $|\mathcal{G}^{\mathrm{P}}|/|\mathcal{G}^{\mathrm{C}}| = 8/4 = 2$ and implies occurrence of two orientational variants. The same result is obtained (see, e.g., [42]) if we restrict ourselves to proper rotations, with the groups $\mathcal{G}^{\mathrm{P}} = 222$ (order 4) and $\mathcal{G}^{\mathrm{C}} = 121$ (order 2), as done here. Note that all the point group symbols refer to the standard symmetry directions (viewing direction) for orthorhombic symmetry, taken also for monoclinic and triclinic symmetry, accentuated by the "1"s in the point group symbols.

In the sense of [40], however, two orientational variants are only expected if $|\mathcal{G}^{\mathrm{P}}|/|\mathcal{H}| = 4/2 = 2$ holds, and requiring $\mathcal{H} = \mathcal{G}^{\mathrm{C}} = 121$ and thus coinciding twofold axes, i.e., $\mathbf{b}'_{\eta'} \| \pm \mathbf{b}_{\eta}$. If the OR, however, implies a (likely small) deviation from $\mathbf{b}'_{\eta'} \| \pm \mathbf{b}_{\eta}$, the intersection group becomes triclinic, $\mathcal{H} = 111$ and $|\mathcal{G}^{\mathrm{P}}|/|\mathcal{H}| = 4/1 = 4$, implying that four η′ child variants are expected.

In line with the convention of the MTEX software, the orientation $\mathbf{O}^{\mathrm{P}}$ of a parent and the orientation $\mathbf{O}^{\mathrm{C}}$ of a child crystallite are the matrices realizing the basis transformation from the parent/child to the specimen coordinate system. E.g. a three-component column vector $\mathbf{r}^{\mathrm{P}}$ in parent crystal coordinates transforms into a three-component column vector $\mathbf{r}^{\mathrm{s}}$ in specimen coordinates:

$$\mathbf{r}^{\mathrm{s}} = \mathbf{O}^{\mathrm{P}} \mathbf{r}^{\mathrm{P}} \tag{1}$$

A misorientation between parent orientation $\mathbf{O}^P$ and child orientation $\mathbf{O}^C$ is described by the matrix $\mathbf{D}^{PC}$ that realizes the basis transformation from parent to child coordinates, i.e.,

$$\mathbf{r}^C = \left(\mathbf{O}^C\right)^{-1}\mathbf{r}^s = \left(\mathbf{O}^C\right)^{-1}\mathbf{O}^P\mathbf{r}^P = \mathbf{D}^{PC}\mathbf{r}^P \tag{2}$$

Application of the point group operations $\mathbf{S}^{P(v)}$ and $\mathbf{S}^{C(v')}$ leads to the $4 \times 2 = 8$ misorientation matrices $\mathbf{D}^{P(v)C(v')}$:

$$\mathbf{D}^{P(v)C(v')} = \mathbf{S}^{C(v)}\mathbf{D}^{P(1)C(1)}\left(\mathbf{S}^{P(v)}\right)^{-1}. \tag{3}$$

Hence, $\mathbf{D}^{PC} \equiv \mathbf{D}^{P(1)C(1)} = \left(\mathbf{O}^{C(1)}\right)^{-1}\mathbf{O}^{P(1)}$ acts as some kind of principal OR associated with the identity operations. The point group operations $\mathbf{S}^{C(1)}$ and $\mathbf{S}^{P(1)}$ are associated with the identity operations of the respective point groups. The matrices $\mathbf{D}^{P(v)C(v')}$ generated in Equation (3) describe the orientations of the child variants with respect to a given parent crystal. The IDs of the variant indices v and v' run over the symmetry elements of the respective symmetry group ($v = 1, \ldots, 4$ for P and $v' = 1, \ldots, 2$ for C, in the present case). By application of those symmetry operations of the point groups of the parent phase, which are *not* elements of the intersection group $\mathcal{H}$, give rise to *up to* four distinguishable orientational variants if $\mathcal{H} = 111$ (see above).

3.2. Habit Planes

Frequently, child-phase crystals assume a plate-like morphology in a parent phase matrix. The idealized plane of the plates is commonly referred to as the habit plane. The habit plane normals (three-component column unit vectors) can be described in specimen coordinates by the $\hat{\mathbf{h}}^S$, in parent crystal coordinates by $\hat{\mathbf{h}}^P$, and in child crystal coordinates by $\hat{\mathbf{h}}^C$. Since crystal coordinates are well defined only up to symmetry, symmetrically equivalent representations of the lattice plane have to be considered. It has been observed that for polycrystalline transformation, microstructures of specific systems that habit planes in crystal coordinates are characteristic. In view of the 222 point group symmetry of the parent phase, there are in general four planes $\hat{\mathbf{h}}^{P(v)}$ which can be generated from a given normal $\hat{\mathbf{h}}^{P(1)} \equiv \hat{\mathbf{h}}^P$:

$$\hat{\mathbf{h}}^{P(v)} = \left(\mathbf{S}^{P(v)}\right)^{-1}\hat{\mathbf{h}}^{P(1)}. \tag{4}$$

Degeneracy occurs if $\hat{\mathbf{h}}^{P(v)}$ is parallel to any twofold axes. In terms of Miller indices, these planes correspond to $(hkl)_P$, $\left(h\bar{k}\bar{l}\right)_P$, $\left(\bar{h}k\bar{l}\right)_P$, and $\left(\bar{h}\bar{k}l\right)_P$.

Moreover, the 121 symmetry of the child crystals implies that there are, in general, two planes $\hat{\mathbf{h}}^{C(v)}$:

$$\hat{\mathbf{h}}^{C(v)} = \left(\mathbf{S}^{C(v)}\right)^{-1}\hat{\mathbf{h}}^{C(1)}. \tag{5}$$

These correspond to $(hkl)_C$ and $(\bar{h}k\bar{l})_C$. In the general case of an intersection group $\mathcal{H} = 111$, only one of these 2 vectors coincide to a $\hat{\mathbf{h}}^{P(v)}$ in view of the OR, whereas in the special case of $\mathcal{H} = 121$, both have counterparts. In the present general case, the $\mathcal{H} = 111$ applies, meaning that no symmetry elements of the two crystals η and η′ are in common. Consequently, a fixed η′ habit plane should occur parallel to a fixed η habit plane.

4. Results

4.1. General Appearance of the Microstructure

As revealed by imaging using backscattered electrons in the SEM, the powder particles contain two distinct types of regions slightly differing by the backscattered intensity (dark and light grey in Figure 2), which becomes visible by appropriate detector settings. In

a given particle, the darker regions are bounded by up to four different types of traces which can be attributed to four types of planes (see Figure 2c). Hence, in line with the considerations from Section 3.2, the dark regions can be regarded as the η′ phase with its predicted four different habit planes in a lighter η-phase matrix. This is also confirmed by the EBSD analyses described below. The plates of the η′ phase show tapered ends close to plate intersections, rounded intersections between the intersecting plates, and modulations of non-intersecting plates close to intersections (see Figure 2d) which is indicative for minimization of the strain energy [43–46] in the two-phase microstructure.
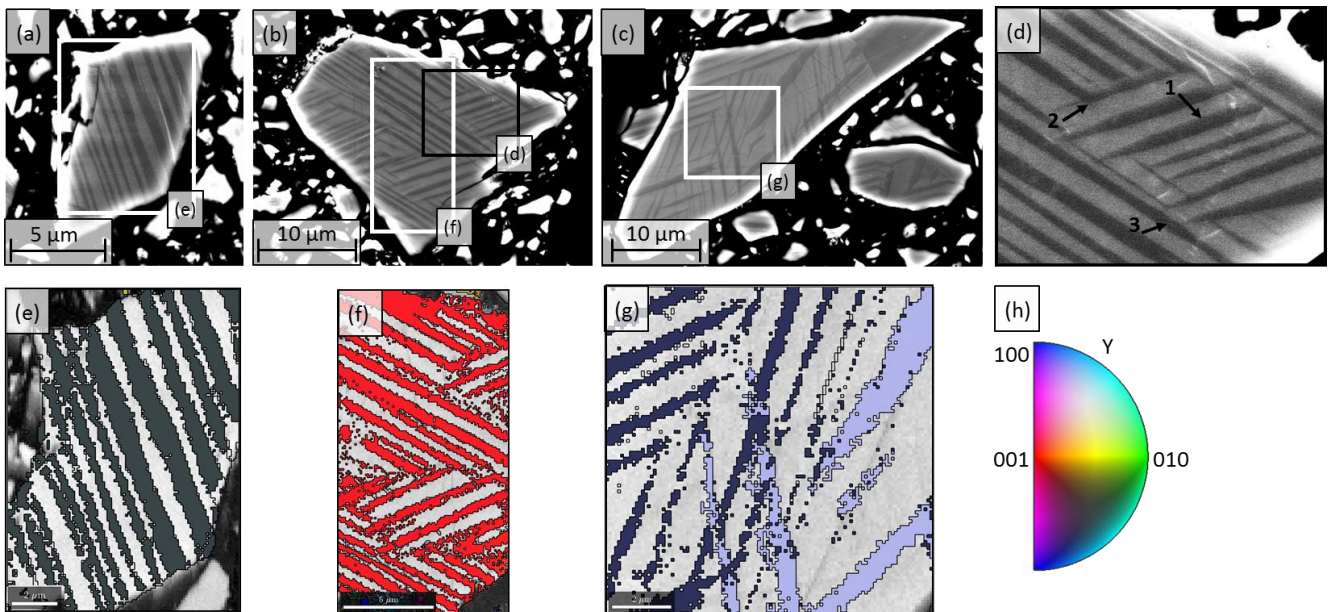

Figure 2. (**a–c**) Backscattered electron contrast image of the cross sections of powder particles with dark plates of the η′ phase in a lighter η matrix. (**d**) Typical characteristics of the bands in detail. 1—tapered ends close to plate intersections, 2—rounded intersections between the plates, 3—modulations of non-intersecting plates close to intersections. (**e–g**) The corresponding EBSD maps after final indexing. The η matrix is shown in EBSD band contrast (gray scale). The plates consisting of η′ phase are indexed using the pseudo-orthorhombic subcell given in Table 2 and are colored according to inverse pole-figure (IPF) color code in (**h**) with respect to the **y** direction of the maps.

4.2. Basic Evaluation of EBSD Data

4.2.1. Phase Distinction and Orientation Determination

Exemplary EBSD patterns of the η (η‴) matrix and an η′ variant are shown in Figure 3. The visible Kikuchi bands correspond to the fundamental reflections, such that these are available for phase and orientation separation. Kikuchi bands corresponding to superstructure/satellite reflections of η′ and η‴ are not clearly visible above the background which is explainable by their low expected intensity. Therefore, the Kikuchi bands of superstructure/satellite cannot be detected by the Hough-space algorithm and are not available for the distinction between the different phases and their orientations during indexing.

The EBSD patterns shown in Figure 3 appear to be very similar. However, the intensity difference images calculated from EBSD patterns from adjacent points in the microstructure reveals slightly different positions of the Kikuchi bands originating from the metric difference of the neighboring orthorhombic and monoclinic (pseudo-orthorhombic) crystal structures of η and η′ (see analysis in Appendix B) and due to an additional rotation according to a small deviation from $\mathbf{b}'_{η'} \| \mathbf{b}_η$.

An accurate detection of the position of the Kikuchi bands and careful calibration are required to achieve a correct indexing result. An example of the effect of slight variation

of the projection center coordinates PCX and PCY is shown in Figure 4. Hence, in this case, the fully automated or semi-automated software calibration provides reasonable starting parameters but not necessarily the best choice, which makes re-indexing with slightly varying calibration parameters inevitable. Statistically predominantly correct phase separation and identification of the domain orientations after careful calibration is possible. However, as it will be evident from the results, some misindexing cannot be eliminated.
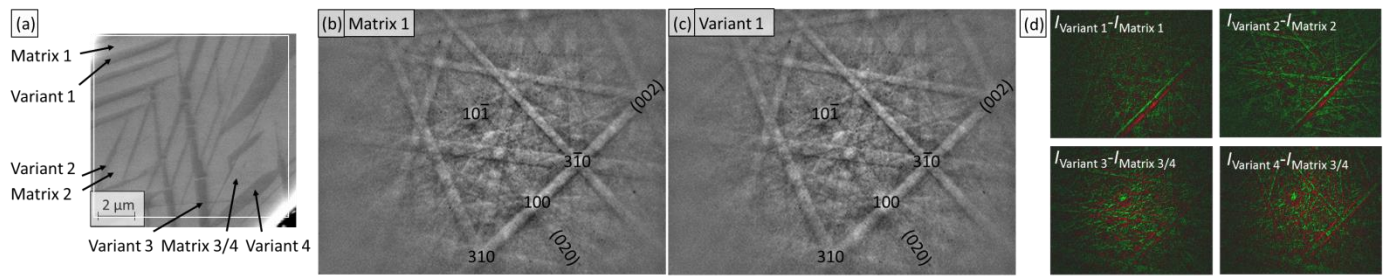

Figure 3. (**a**) Backscattered electron contrast image of the particle shown in Figure 2c. The four different variants and directly neighboring matrix regions are labeled. (**b,c**) Experimental EBSD patterns of the matrix 1 and variant 1 region averaged over 24 EBSD patterns. (**d**) Intensity difference images from experimental EBSD patterns of the regions indicated in (**a**). (Green: Intensity is higher in the EBSD pattern of the variant, Red: Vice versa).
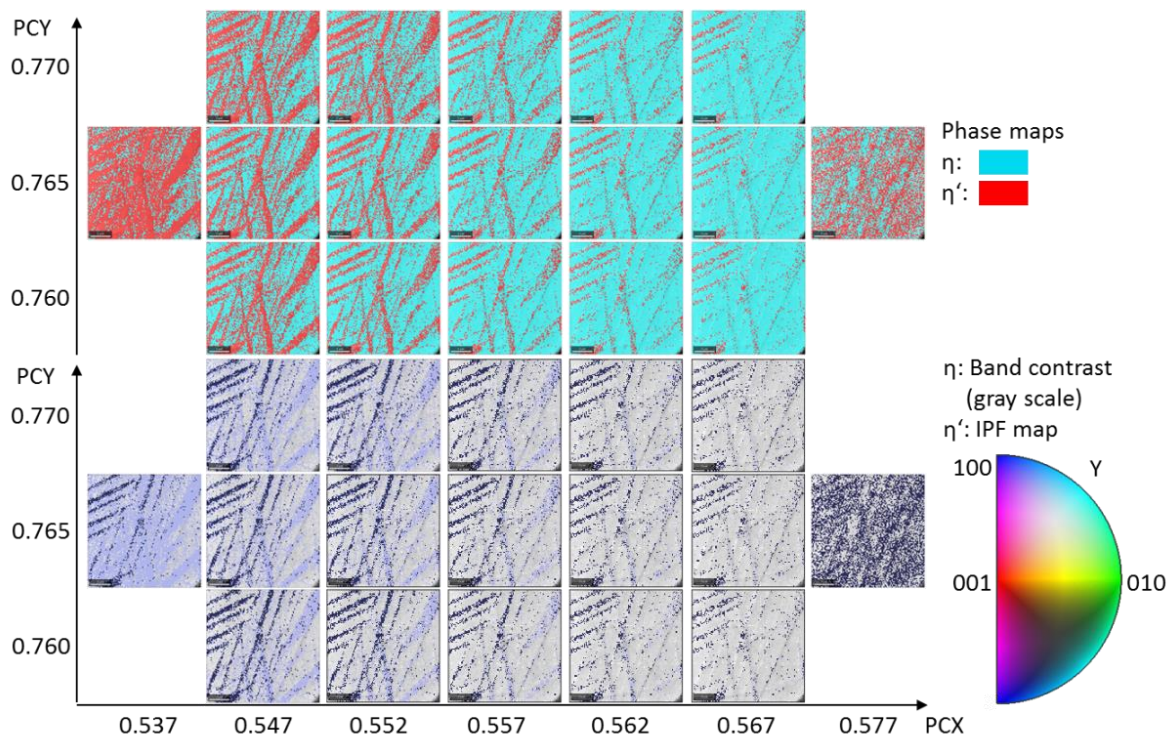

Figure 4. Effect of varying the projection center coordinates PCX and PCY on the indexing result. The significance of choosing the correct projection center is shown for phase separation and identification of the domain orientations. Note that for all tested values for the projection center calibration, the whole map is indexed with a high reliability. The phases in the upper map are colored according to the indicated color code. In the lower orientation maps, the η phase is presented referring to the band contrast while the η' phase is colored according to inverse pole-figure (IPF) color code with respect to the **y** direction of the maps.

4.2.2. Orientation Distribution, Orientation Relationships and Misorientations

Generally, the η-matrix orientations of the particles show very narrow orientation distributions (Figure 5a), spreading in a given particle about $\pm 0.5°$ around the mean orientation. In view of orientation noise, this corresponds to the minimal achievable precision of an EBSD measurement which is given to be between 0.5° and 2° for Hough-space based orientation determination, depending on the experimental conditions and data-analysis procedures [47]. A more than 10-times higher precision is achievable using the pattern matching approach [47,48]. It was decided, however, to employ the much more accessible Hough-space based methods in the present work.

The orientation distribution of the variant orientations is shown in Figure 5b–d (see also [42]). In order to present the four variant orientations together in a single graph, the variant orientations are shown with respect to the center of the fundamental region. Although they are overlapping to some degree, the orientations of the variants are clearly distinct. This illustrates the additional symmetry break according to the ideal lattice correspondence due to the optimization of the accommodation process leading to $\mathcal{H} = 111$ (see Section 3).

The principal $\mathbf{D}^{PC}$ is estimated from the experimental parent orientations $\mathbf{O}^P(n)$ and child orientations $\mathbf{O}^C(n)$ by optimizing the fit [49]:

$$\sum_{n=1}^{N} \omega\left(\mathbf{O}^P(n), \mathbf{O}^C(n)\mathbf{D}^{PC}\right)^2. \tag{6}$$

This results in the misorientation matrix:

$$\mathbf{D}^{PC} = \begin{pmatrix} 1.0000 & -0.00045 & -0.00360 \\ 0.00044 & 0.99999 & 0.00471 \\ -0.00360 & -0.00471 & 0.99998 \end{pmatrix} \tag{7}$$

which deviates from identity matrix by 0.34°. Basically, this corresponds to close-to parallelism of the lattice basis vectors according to Table 2.
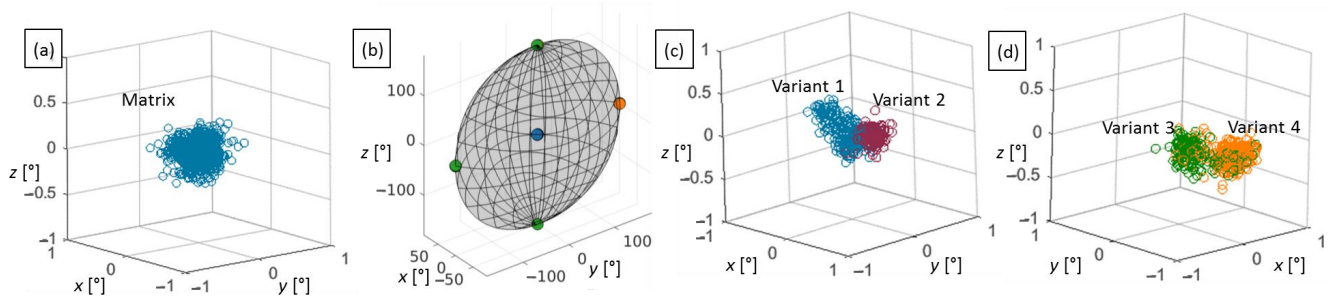

Figure 5. EBSD based orientation analysis from the η/η′ powder particle shown in Figure 2c using the axis-angle orientation space [42], where the distance from the origin corresponds to the misorientation angle, and the direction corresponds to the misorientation axis of the orientation with respect to the reference orientation. Reference orientation is the average orientation of the orientation points shown in cases (**a**,**c**,**d**), whereas it is the average matrix orientation in (**b**). The η matrix (**a**) and the η′ variants (**b**) are shown schematically, where the four points at the boundaries of the fundamental zone actually correspond to one double orientation cluster as visible in (**d**). The small orientation differences between pairs of the four domain variants are highlighted in (**c**,**d**). These pairs in (**c**,**d**) differ from each other by a rotation of 180°, e.g., around $\hat{\mathbf{e}}_3^C$ (Figure 1) visible in (**b**).

4.3. Habit Plane Determination

Upon analyzing a two-dimensional section through a microstructure containing parent crystals containing child variants, the habit planes are visible in the measurement surface

in terms of their traces. These traces, in turn, can be used to deduce preferentially occurring habit planes.

4.3.1. Determination of Traces

To determine the habit planes between parent (P) η and child (C) η′ variants, traces $\hat{\mathbf{r}}^S(n)$ with respect to the specimen coordinate system are measured from differently oriented particles. These traces can be taken as unit vectors in the sample surfaces. Hence these are uniquely determined by an angle α leading to $\hat{\mathbf{r}}^S(n) = \begin{pmatrix} \cos\alpha & \sin\alpha & 0 \end{pmatrix}$ (compare Figures 6 and A2 in Appendix C).

The accuracy with which the indices of the trace can be determined is discussed in Appendix C. Considering all the sources impairing the accuracy of a measured trace, one should be aware that the actual traces are at least approx. $\pm 5°$ off from the measured trace.
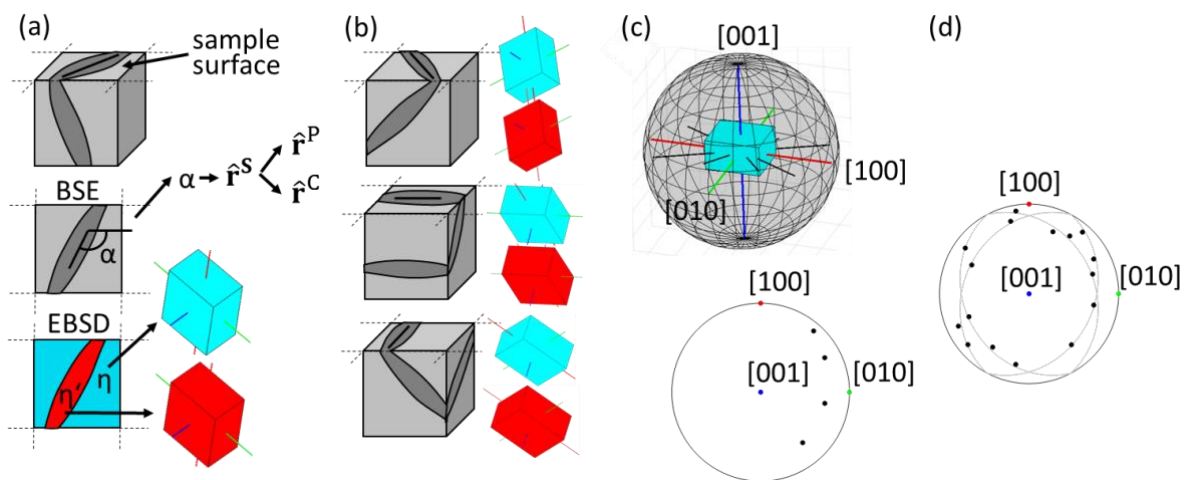

Figure 6. Schematic illustration of the procedure of determining the habit plane of a microstructural feature from metallographic cross sections and EBSD data. (**a**) Traces $\hat{\mathbf{r}}$ of plate-like precipitate on the sample surface which is available for the microscopic investigation. The position of the trace in terms of α and the crystallographic orientation are, thus, determined. (**b**) Traces $\hat{\mathbf{r}}^S$ for various orientations of the sample with respect to the sample surface should be detected. (**c**) The measured traces $\hat{\mathbf{r}}^S$ expressed as [*uvw*] lie within the habit plane {*hkl*} and appear as big circles in a stereographic projection. For illustration purposes the four traces from (**a**,**b**) belonging to a specific habit plane (*hkl*) are shown. (**d**) Usually, measured traces belong to all habit planes, be they crystallographically equivalent or different. As an illustration of this, traces and corresponding big circles are shown for four equivalent habit planes of the orthorhombic crystal structure of the η phase. The big circles of the habit planes are shown as gray lines in the stereographic projection.

4.3.2. Pure Evaluation of Traces

In order to determine a habit plane from the traces $\hat{\mathbf{r}}^S(n)$ that are measured from differently oriented grains (Figure 6b), normal vectors $\hat{\mathbf{h}}^{P(v)}(n)$ and $\hat{\mathbf{h}}^{C(v)}(n)$ that are best orthogonal to all these traces are looked for. That requires that the trace vectors are transformed into the coordinate systems of the parent/child crystals adjacent to the trace for which the direction is given:

$$\hat{\mathbf{r}}^P(n) = \left(\mathbf{O}^P(n)\right)^{-1}\hat{\mathbf{r}}^S(n) \tag{8a}$$

$$\hat{\mathbf{r}}^C(n) = \left(\mathbf{O}^C(n)\right)^{-1}\hat{\mathbf{r}}^S(n) \tag{8b}$$

where $\mathbf{O}^P(n)$ and $\mathbf{O}^C(n)$ are parent and child orientations, respectively (Figure 7a,b).

From these transformed traces, the best orthogonal vector $\hat{\mathbf{h}}^P$ can be found describing the habit plane as a solution of the following optimization problem:

$$\chi^2(\hat{\mathbf{h}}^P) = \frac{1}{N} \sum_{n=1}^{N} \left(90° - \omega(\hat{\mathbf{r}}^P(n), \hat{h}^P)\right)^2 \rightarrow min. \tag{9a}$$

$$\omega(\hat{\mathbf{r}}^P(n), \hat{\mathbf{h}}^P) = \min_v \arccos(\hat{\mathbf{r}}^P \hat{\mathbf{h}}^{P(v)}) \tag{9b}$$

Equation (9b) thus denotes the smallest angle between the trace $\hat{\mathbf{r}}^P(n)$ and any of the planes $\hat{\mathbf{h}}^{P(v)}$ symmetrically equivalent to $\hat{\mathbf{h}}^P$. The functional $\chi^2(\hat{\mathbf{h}}^P)$ is the squared angular deviation of the traces from a trial habit plane $\hat{\mathbf{h}}^P$. Details on the chosen exponent are presented in the Appendix D.

The functional $\chi^2(\hat{\mathbf{h}}^P)$ is plotted in Figure 7d where the minima are marked. Ideally, it would be expected that all measured traces in Figure 7a are exactly in the big circle pertaining to the habit plane $\hat{\mathbf{h}}^P$. In fact, they are scattered around four circles which correspond to the four symmetrically equivalent habit planes $\hat{\mathbf{h}}^{P(v)}$. The habit plane of the orthorhombic η phase results in $\{hkl\}_\eta = \{1\,1.6\,2.2\}_\eta$ with $\sqrt[2]{\chi^2} = 2.4°$ as included in Table 3.
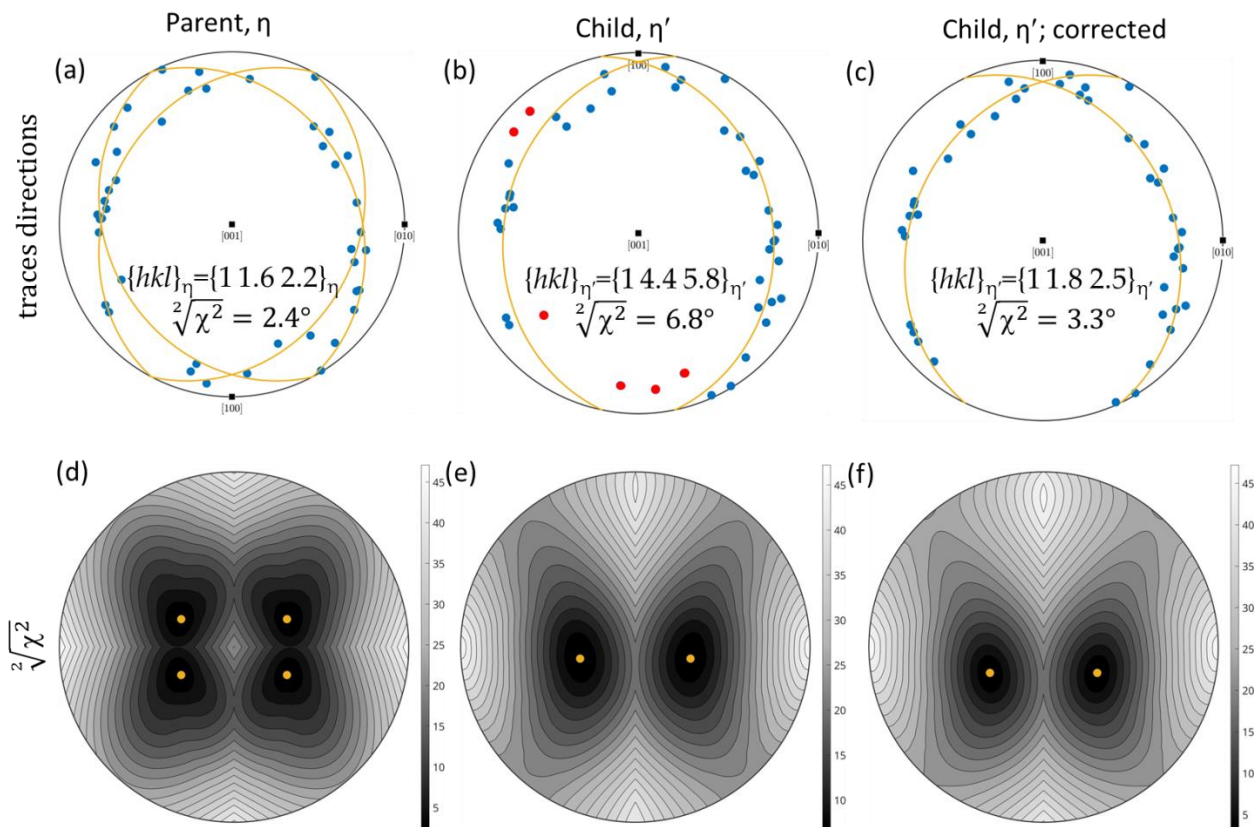

Figure 7. Separate analysis of the directions of the habit plane traces for the parent (P; η) and child (C; η′) depicting stereographic projections illustrating (**a**) the parent traces $\hat{\mathbf{r}}^P(n)$ and (**b**) the child traces $\hat{\mathbf{r}}^C(n)$, determined via Equation (8a,b). The big circles pertaining to the four equivalent habit planes $\hat{\mathbf{h}}^P$ and two equivalent habit planes $\hat{\mathbf{h}}^P$ are indicated. Traces deviating by more than 5° from the big circles in (**b**) are marked in red. After replacement of those traces by their pseudosymmetric counterparts, all child traces are located on the two big circles (**c**). The {hkl} from χ^2 minimization are given in (**a**–**c**). Diagrams (**d**–**f**) illustrate the corresponding direction-dependent value $\sqrt[2]{\chi^2}$. The orange points indicate the determined habit plane poles at the minimum related to the symmetry element of the crystal class, i.e., the considered rotational point groups + inversion: *mmm* (parent) and 12/*m*1 (child). Note the shift of $\sqrt[2]{\chi^2}$ minima after correction of child traces (**e**,**f**).

A similar minimization problem can be solved with respect to the child reference system. The corresponding functional $\chi^2(\hat{\mathbf{h}}^C)$ is depicted in Figure 7e together with the optimal habit plane $\hat{\mathbf{h}}^C$. Figure 7b shows how the child traces scatter around two symmetrically equivalent big circles with tentative $\{hkl\}_{\eta'} = \{1\ 4.4\ 5.8\}_{\eta'}$ for $\sqrt[2]{\chi^2} = 6.8°$ as included in Table 3. Assuming a perfect orientation relationship $\mathbf{D}^{PC}$, the preferred habit planes in coordinated parent and child are related via $\hat{\mathbf{h}}^C = \mathbf{D}^{PC}\hat{\mathbf{h}}^P$. However, using the experimental orientation relationship $\mathbf{D}^{PC}$ described in Section 4.2.2, the optimal habit plane $\hat{\mathbf{h}}^C$ deviates from $\mathbf{D}^{PC}\hat{\mathbf{h}}^P$ by 7°.

A minority set of traces, however, appears to scatter around two further great circles inequivalent to the 1 2 1 symmetry. These two minority great circles may be conceived to be generated from the two majority great circles by a rotation of 180° around $\hat{\mathbf{e}}_3^C$ lost by the symmetry reduction from P to C. It appears likely that the traces $\hat{\mathbf{r}}$ on the minority great circles result from misindexing of the η' child phase by this 180° rotation (see Figure 5). For that reason, child orientations corresponding to traces deviating by more than 5° from the big circles were replaced by its pseudosymmetrical counterpart, i.e., by rotating them around $\hat{\mathbf{e}}_3^C$ by about 180°. This affected 6 of 43 orientations. All subsequent calculations are based on that corrected data set. In particular, the traces $\hat{\mathbf{r}}^C$ (Equation (8b)), the parent to child orientation relationship $\mathbf{D}^{PC}$ (Equation (11a,b)) and best fitting habit plane $\hat{\mathbf{h}}^C$ as a solution of the minimization problem 9a are recomputed. The resulting χ^2 plot in Figure 7f shows minima shifted with respect to Figure 7e, corresponding finally to $\{hkl\}_{\eta'} = \{1\ 1.8\ 2.5\}_{\eta'}$ with $\sqrt[2]{\chi^2} = 3.3°$ as included in Table 3. All traces are located on the two majority big circles, as shown in Figure 7c. The habit plane $\hat{\mathbf{h}}^C$ determined from the corrected traces deviates from $\mathbf{D}^{PC}\hat{\mathbf{h}}^P$ by only 1°.

Table 3. Indices of the η (parent, P) habit planes $\{hkl\}_\eta$ and η′ (child, C) habit planes $\{hkl\}_{\eta'}$; angular deviation $\sqrt[2]{\chi^2}$ of the traces from the habit planes; and angular deviation of the habit planes $\hat{\mathbf{h}}^C$ from $\mathbf{D}^{PC}\hat{\mathbf{h}}^P$ determined by the different methods and adjusted data sets. Note that for ease of comparability of habit planes, h is normalized to 1.

Method	$\{hkl\}_\eta$, $\sqrt[2]{\chi^2}$	$\{hkl\}_{\eta'}$, $\sqrt[2]{\chi^2}$	$\measuredangle(\hat{\mathbf{h}}^C, \mathbf{D}^{PC}\hat{\mathbf{h}}^P)$
Pure evaluation of traces			
• As measured traces	$\{1\ 1.6\ 2.2\}_\eta$, 2.4°	$\{1\ 4.4\ 5.8\}_{\eta'}$, 6.8°	7°
• Traces from pseudosymmetry-corrected child orientations	–	$\{1\ 1.8\ 2.5\}_{\eta'}$, 3.3°	1°
Combined evaluation of misorientations and traces			
• Variant IDs v_n and v'_n corrected and • Full information in combined functional	$\{1\ 1.8\ 2.5\}_\eta$, 3.3°	$\{1\ 1.8\ 2.5\}_{\eta'}$, 3.3°	0°

4.3.3. Combined Evaluation of Misorientations and Traces

In the previous section, a set of four symmetrically equivalent big circles for each habit plane had to be considered to be fitted against the parent traces. This does not yet fit the assumption that a unique preferred habit plane exists for the specific orientation relationship. In the present section, we aim to utilize this assumption to project the parent traces on to a unique habit plane before determining it as a solution of the optimization of Equation (9a,b). This will be accomplished by determining the parent and child variant

ID v_n and v'_n for each pair of measured parent orientations $\mathbf{O}^P(n)$ and child orientation $\mathbf{O}^C(n)$.

Due to crystal symmetry, these pairs satisfy the orientation relationship:

$$\mathbf{O}^P(n)\mathbf{S}^{P(v_n)} \approx \mathbf{O}^C(n)\mathbf{S}^{C(v'_n)}\mathbf{D}^{PC} \tag{10}$$

subject to suitably chosen parent and child symmetries $\mathbf{S}^{P(v_n)}$ and $\mathbf{S}^{C(v'_n)}$. For each pair n, the variant IDs v_n and v'_n are determined by minimizing the misfit in Equation (6).

In Figure 8a,d the trace vectors according to the corresponding variant IDs v_n and v'_n are colorized. It is observed that, with some exceptions, the colors separate according to the symmetrically equivalent circles. It can be assumed that the exceptions occur due to incorrectly determined variant IDs v_n and v'_n. This might be explained by the similarity of certain pairs of variants as depicted in Figure 5. In Figure 8a, the traces that deviate by an angle larger than 5° from the fitted habit plane of the assigned variant are marked. For the corresponding parent and child orientations, the variant IDs v_n and v'_n are replaced by the second best fit of Equation (10). The updated variant IDs v_n and v'_n are displayed in Figure 8. Interestingly, the updated parent variant IDs v_n are also more consistent with the four big circles.

The central idea within this section is to replace the experimentally determined parent and child orientations $\mathbf{O}^P(n)$ and $\mathbf{O}^C(n)$ by symmetrically adjusted variants $\mathbf{O}^P(n)\mathbf{S}^{P(v_n)}$ and $\mathbf{O}^C(n)\mathbf{S}^{C(v'_n)}$ that satisfy the orientation relationship $\mathbf{D}^{PC}$ without the need for additional symmetries. Subsequently, the parent traces $\hat{\mathbf{r}}^P$ and child traces $\hat{\mathbf{r}}^C$ (Equation (8a,b)) are adjusted accordingly. Figure 8 shows that after this adjustment, all traces scatter around a single big circle.

The advantage of this procedure is that for the final fitting of the habit plane, symmetrically equivalent versions do not have to be considered; instead, a unique plane normal $\hat{\mathbf{h}}^P$ and $\hat{\mathbf{h}}^C$ is determined that minimizes:

$$\chi^2(\hat{\mathbf{h}}^P) = \frac{1}{N}\sum_{n=1}^{N}\left(90° - \arccos(\hat{\mathbf{r}}^P(n)\hat{\mathbf{h}}^P)\right)^2 \to min, \tag{11a}$$

$$\chi^2(\hat{\mathbf{h}}^C) = \frac{1}{N}\sum_{n=1}^{N}\left(90° - \arccos(\hat{\mathbf{r}}^C(n)\hat{\mathbf{h}}^C)\right)^2 \to min \tag{11b}$$

respectively.

The resulting χ^2 plot in Figure 8f shows a single minimum corresponding to $(hkl)_\eta$ and $(hkl)_{\eta'}$ both with $(1\ 1.8\ 2.5)_{\eta/\eta'}$ and $\sqrt[2]{\chi^2} = 3.3°$. Table 3 cites these results in terms of $\{hkl\}_\eta$ and $\{hkl\}_{\eta'}$.

As evident from the entries in Table 3, this χ is poorer than that obtained upon evaluation without considering the combination of misorientation and trace information. However, without considering the combination of misorientation and trace information, we essentially allow four symmetrically equivalent habit planes per parent/child pair, whereas in the current section we allow only for a single habit plane. This involves fewer degrees of freedom, explaining the poorer fit.

Surprisingly, both minimization problems (Equation (11a,b)) result in almost perfectly agreeing habit planes $\hat{\mathbf{h}}^C$ and $\mathbf{D}^{PC}\hat{\mathbf{h}}^P$. This need not be true in general. In fact, a perfect coincidence of $\hat{\mathbf{h}}^{C(1)} = \mathbf{D}^{PC}\hat{\mathbf{h}}^P$ can be ensured by combining both minimization problems into a single one:

$$\chi^2(\hat{\mathbf{h}}^P) = \frac{1}{N}\sum_{n=1}^{N}\left(90° - \arccos(\hat{\mathbf{r}}^P(n)\hat{\mathbf{h}}^P)\right)^2 + \left(90° - \arccos(\hat{\mathbf{r}}^C(n)\mathbf{D}^{PC}\hat{\mathbf{h}}^P)\right)^2 \to min \tag{12}$$

Minimizing this functional eventually makes use of the full information which was collected during the measurements, i.e., all parent and child orientations and the determined parent and child variants. In the present case, minimizing the combined functional gives the same result as above.
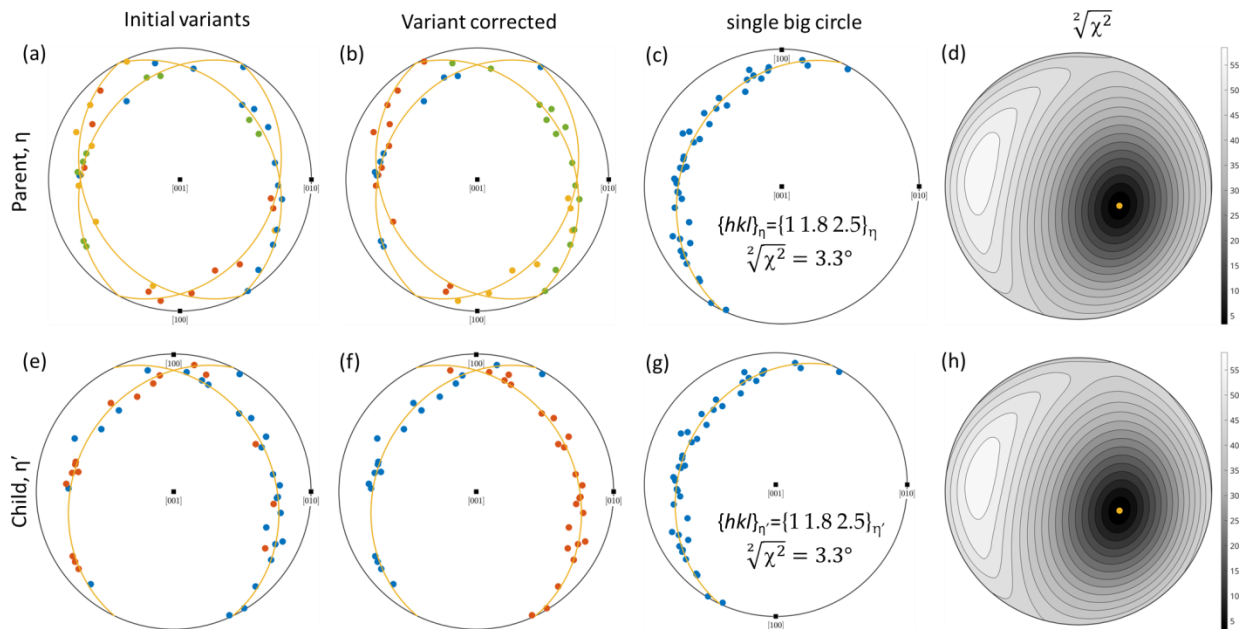

Figure 8. Stereographic projection of the measured traces (points) and habit planes (big circles) determined by the combined evaluation of misorientations and traces for the orthorhombic η phase (**a**–**c**) and the pseudo-orthorhombic η′ phase (**d**–**f**). The trace points are colored according to the parent and child variant ID v_n and v'_n due to the chosen parent and child symmetries $\mathbf{S}^{P(v_n)}$ and $\mathbf{S}^{C(v'_n)}$ derived from optimizing Equation (10). Diagrams (**a**,**d**) show the traces of η′ and η colored according to their parent and child variant ID v_n and v'_n. In (**b**,**f**), an additional correction for pseudosymmetry is applied. The variant-adjusted traces in (**c**,**g**) show a good fit to a single big circle. The (*hkl*) from χ^2 minimization are given in (**c**,**g**). In (**d**,**h**), the direction-dependent value $\sqrt[2]{\chi^2}$ is illustrated after mapping all traces onto a single big circle. The orange points indicate the determined habit plane poles at the minimum.

5. Discussion

5.1. Implications for the Al$_5$Fe$_2$ Intermetallic

As expected for an order–disorder transformation accompanied by a small transformation strain, the invariant substructures are mutually virtually oriented in parallel as reflected by the orientation relationship $\mathbf{D}^{PC}$. The habit plane developing between η and η′ is expected to be optimized according to some geometric/energetic criteria. These theories have been developed addressing precipitation [50] or martensite transformation [46,51], in particular involving means to reduce the metrical misfit between the phases across the interface. Attempts to interpret the observed habit plane orientation with such a minimum misfit in view of the transformation strain $\varepsilon_{\eta\to\eta'}$ (see Equations (A3) and (A4) in Appendix B) were, however, unsuccessful. It might be speculated that anisotropic thermal expansion might occur between the treatment temperature of 250 °C (at which the microstructure develops) and room temperature (at which the X-ray diffraction experiments have been carried out, for determination of $\varepsilon_{\eta\to\eta'}$). Hence, it could render the value of $\varepsilon_{\eta\to\eta'}$ to be different from that acting during the transformation and determining the microstructure.

Formation of the two-phase microstructure η + η′ investigated in the present work is, in any case, expected to reduce the toughness of the intermetallic. η-Al_5Fe_2 is known to be brittle at 500 °C (and below), while ductility is only observed above 600 °C [52]. Hence, the structural inhomogeneity induced by the transformation is expected to cause local stress concentrations, e.g., at the edges of the lens-shaped particles, which can initiate crack formation. Sufficiently rapid cooling of η having developed at higher temperature may suppress η′ formation and improve toughness of this intermetallic.

5.2. Utilization the Combined Evaluation of Misorientations and Traces for Habit Plane Analysis

Two-dimensional scanning EBSD analysis on largely ordinary metallographic specimens has strongly extended the possibilities offered by conventional scanning electron microscopy investigations on such specimens. First of all, it is possible to discriminate the phase and determine its crystallographic orientation, and, thus, also the misorientation of adjacent identical or dissimilar crystals, i.e., the OR. While that type of analysis has become a routine procedure, determination of certain real-space features like the interface (habit) planes is less frequently conducted. This has two obvious reasons:

(a) Orientations of real-space features suffer from all types of image distortions [53]. The systematic distortion effects cancel out upon determination of misorientations of, e.g., adjacent crystallites, whereas the measurable orientation of real-space features like traces of habit planes are fully affected by these distortions. See Appendix C for an assessment of these errors for the present data.

(b) As it concerns habit planes (and other planar features), the usual two-dimensional sections do not directly reveal the complete plane orientation, because the inclination angle of the habit plane with respect to the specimen surface is not directly available. Solutions to this problem can be as follows:

    (i) The classical two-trace analysis applied on one and the same feature [54], applied to a specimen having a suitable geometry or which has been brought into suitable geometry [55–57]. Habit plane determination in the course of the combination of EBSD with three-dimensional sectioning has to be regarded as a special case of this two-section method, where the corresponding information becomes available automatically [58–60].

    (ii) Use of two-dimensional data in connection with guessed (likely low-index) or predicted (by some appropriate theory, like the phenomenological theory of martensite crystallography) habit planes, allowing for calculation of trace orientations which can be compared with the experimental trace orientation. A sufficient number of observed traces must agree within the experiment so as to regard the guess or prediction as confirmed. This method is definitely a routine and very common method with much more numerous examples being around than cited for (i).

    (iii) Plot experimentally determined trace orientations in the crystal coordinates of one of the two crystals separated by the habit plane (possibly affected by the above-mentioned errors) into a stereographic projection, which then should follow a set of symmetry-equivalent big circles of the habit plane. As with method (ii), this procedure is only applicable if a low numbered set of habit planes dominates in the specimen. Consequently, this method is not suitable for specimens with more or less varying habit planes, such as more or less random grain boundaries in single-phase polycrystals. Note that the stereological method known as the five-parameter analysis used to determine full boundary plane *distributions* is applicable for sufficiently large 2D EBSD maps of reasonably high indexing quality [61,62] and encompasses all interfaces, not only a limited number of specific ones. Method (iii) has succeeded in the present work, as shown in Section 4.3.2 and leading to Figure 7. This success was made possible by the low orthorhombic and monoclinic symmetries of the η and η′ phases investigated in the present study, with four

or two habit planes equivalent by symmetry. In case of higher symmetry, like cubic $m\bar{3}m$ (or rotation group 432), one expects the traces to be distributed on 24 big circles of the 24 symmetry-equivalent habit planes. These may be distributed so densely over the stereographic projection that the scatter does not allow clear identification of the big circles. The situation is more favorable if the habit planes assume high-symmetry orientations, allowing, e.g., identification of {110} habit planes of crystallites of a cubic phase using this method [63].

(iv) The method applied in Section 4.3.3 and leading to Figure 8 (which might be conceived as a method (iv)), using simultaneously crystal orientation and trace information, is generally applicable, if a single orientation relationship predominantly occurs between identifiable pairs of crystals (of the same or different phases) in connection with a dominant habit plane. A dominant habit plane then implies that the plane orientation (here $\hat{\mathbf{h}}^P$ and $\hat{\mathbf{h}}^C$ for two distinct parent and child phases) is fixed in both crystals. In that case the information of the traces can be combined with that on the orientation relationship between the two crystal, thus overcoming the necessity to consider up to 24 big circles in the case of high crystal symmetry. Hence, this method can serve as a new tool allowing for determination of re-occurring habit planes based on two-dimensional EBSD data.

6. Summary and Conclusions

The microstructure developing upon formation of monoclinically ordered and plate-like η'-Al_8Fe_3 within a matrix of orthorhombic η-Al_5Fe_2 has been investigated on two-dimensional cross sections of corresponding polycrystalline material. The two different phases and the main distinguishable orientations of the η' phase could be discriminated between, based on slight distortions in the electron backscatter diffraction (EBSD) patterns caused by the transformation strain $\eta \rightarrow \eta'$, using Hough-space based indexing methods. Four different orientations of η' within η were identified, which assume also four different (but symmetry equivalent, as confirmed below) habit planes with respect to the η matrix. The work focused on the determination of the characteristic habit planes for η and η' using two methods, both relying on a series of trace directions:

I The trace directions in crystal coordinates of η and η' assemble around a set of four (η), respectively two (η'), big circles corresponding to a set of symmetry invariant habit plane poles.

II Requiring that for a given orientation of η' with respect to η, having no symmetry elements of the two crystals in common, there should be a fixed η' habit plane parallel to a fixed η habit plane.

By using the latter strategy, the determined traces should be compatible with the respective orientation relationship. This requirement allows, in the present case, to identify η' domains which have been misindexed due to the severe pseudosymmetry. It is suggested, furthermore, that this method can be used in high-symmetry crystal systems with many different orientation variants to unequivocally identify the habit planes.

The most reliable habit planes in η and η' both have indices {1 1.8 2.5}$_{\eta/\eta'}$ within an angular deviation of 3.3°. In view of the inevitable brittle character of the intermetallic, it is expected that formation η' is detrimental for the toughness of the Al_5Fe_2 intermetallic, e.g., in the joining zones that develop between iron/steel and aluminum alloys.

Author Contributions: Conceptualization, H.B., R.H. and A.L.; methodology, H.B., R.H. and A.L.; software, H.B. and R.H.; validation, H.B. and A.L.; formal analysis, H.B.; investigation, H.B.; resources, R.H. and A.L.; data curation, H.B.; writing—original draft preparation, H.B., R.H. and A.L.; writing—review and editing, H.B., R.H. and A.L.; visualization, H.B. and R.H.; supervision, A.L.; project administration, H.B. and A.L.; funding acquisition, H.B. and A.L. All authors have read and agreed to the published version of the manuscript.

Institutional Review Board Statement: Not applicable.

Informed Consent Statement: Not applicable.

Data Availability Statement: All data and MTEX scripts used to determine the habit planes and generate the Figures 7, 8 and A3 are freely available at https://github.com/mtex-toolbox/mtex-paper/tree/master/EtaHabitPlane (accessed on 7 May 2022).

Conflicts of Interest: The authors declare no conflict of interest. The funders had no role in the design of the study; in the collection, analyses, or interpretation of data; in the writing of the manuscript; or in the decision to publish the results.

Appendix A. Structure Models

Table A1. Structure models of the pseudo-orthorhombic η' and orthorhombic η'''/η phase as used for indexing of EBSD patterns. Atomic positions are adopted from the crystal structure model of the disordered η-Al_5Fe_2 by Burkhardt [33] and were used for both phases to receive reflectors in the same order with similar intensities for indexing.

Phase	Subcell	Space Group	Site	Wyckoff Label	Atomic Position x	Atomic Position y	Atomic Position z	Occupation
H''' (η)	Orthorhombic	$Cmcm$	Al(1)	8g	0.188	0.1467	0.25	0.32
			Al(2)	4b	0	0.5	0	0.24
			Al(3)	8f	0.24	0	0.534	1
			Fe(1)	4c	0	0.8277	0.25	1
H'	Monoclinic/Pseudo-orthorhombic	$C2/c$	Al(1)	8f	0.188	0.1467	0.25	0.32
			Al(2)	4b	0	0.5	0	0.24
			Al(3)	8f	0.24	0	0.534	1
			Fe(1)	4e	0	0.8277	0.25	1

Appendix B. Transformation Strain

Note that the following considerations can be made without reference to the actual orientation relationship. It turns out that distinction between η and η' phase and between the latter's variants by evaluation of the EBSD patterns will largely be based on the distortion of these patterns which is strongly connected with the transformation strains. The strain associated with the transformation from η to η', or to be more accurate, the strain which relates the crystal structures in the two-phase microstructure $\eta + \eta'$ to the lattice parameters listed in Table 2, can be calculated making use of an orthonormal coordinate system spanned by $\hat{\mathbf{e}}_1$, $\hat{\mathbf{e}}_2$ and $\hat{\mathbf{e}}_3$ (not directly related to the coordinate systems from Section 3). The basis vectors of the η phase can be formulated within a matrix $\mathbf{M}_\eta^{-T}$ (inverse transpose of $\mathbf{M}_\eta$ as formulated in [64]):

$$\begin{pmatrix} \mathbf{a}_\eta & \mathbf{b}_\eta & \mathbf{c}_\eta \end{pmatrix} = \begin{pmatrix} a_\eta & 0 & 0 \\ 0 & b_\eta & 0 \\ 0 & 0 & c_\eta \end{pmatrix} \begin{pmatrix} \hat{\mathbf{e}}_1 & \hat{\mathbf{e}}_2 & \hat{\mathbf{e}}_3 \end{pmatrix} = \mathbf{M}_\eta^{-T} \begin{pmatrix} \hat{\mathbf{e}}_1 & \hat{\mathbf{e}}_2 & \hat{\mathbf{e}}_3 \end{pmatrix} \quad (A1)$$

The basis vectors for the η phase can be transformed to the chosen pseudo-orthorhombic subcell of the η' phase by a symmetric stretch:

$$\begin{pmatrix} \mathbf{a}'_{\eta'} & \mathbf{b}'_{\eta'} & \mathbf{c}'_{\eta'} \end{pmatrix} = (\mathbf{I} + \boldsymbol{\varepsilon}_{\eta \to \eta'})\begin{pmatrix} \mathbf{a}_{\eta} & \mathbf{b}_{\eta} & \mathbf{c}_{\eta} \end{pmatrix}. \tag{A2}$$

where $\mathbf{I}$ is the identity matrix and $\mathbf{I} + \boldsymbol{\varepsilon}_{\eta \to \eta'}$ is the symmetric stretch tensor, corresponding to the Bain tensor formulated for martensitic transformations [65], and where $\boldsymbol{\varepsilon}_{\eta \to \eta'}$ is a symmetric strain tensor. Solving Equation (3) numerically starting from $\mathbf{b}'_{\eta'} \| \mathbf{b}_{\eta}$ and approximately parallel $\mathbf{a}$ and $\mathbf{c}$ axes, thus with non-zero 11, 22, 33 and 13 components, one obtains:

$$\boldsymbol{\varepsilon}_{\eta \to \eta'} = \begin{pmatrix} 0.00849 & 0 & -0.00399 \\ 0 & 0.00272 & 0 \\ -0.00399 & 0 & -0.01680 \end{pmatrix} = \boldsymbol{\varepsilon}_{\eta \to \eta_1'}. \tag{A3}$$

This strain is relabeled $\boldsymbol{\varepsilon}_{\eta \to \eta_1'}$ because it is only one of two possibilities to obtain the η' unit cell by a *symmetric* stretch from η (compare Figure 1c vs. Figure 1d). The second possibility is obtained if one considers $\mathbf{b}'_{\eta'} \to -\mathbf{b}'_{\eta'}$ and $\mathbf{a}'_{\eta'} \to -\mathbf{a}'_{\eta'}$, corresponding to a 180° rotation of the η' structure around $\hat{\mathbf{e}}_3$ (see Figure 1). The corresponding strain can, e.g., be obtained by transformation of $\boldsymbol{\varepsilon}_{\eta \to \eta_1'}$ by this rotation:

$$\boldsymbol{\varepsilon}_{\eta \to \eta_2'} = \begin{pmatrix} 0.00849 & 0 & +0.00399 \\ 0 & 0.00272 & 0 \\ +0.00399 & 0 & -0.01680 \end{pmatrix}. \tag{A4}$$

The number of these strain tensors is a consequence of the ratio of $|\mathcal{G}^P|/|\mathcal{G}^C| = 2$, although they do not need to correspond to the number of actual orientational variants (allowing deviation from $\mathbf{b}'_{\eta'} \| \mathbf{b}_{\eta}$). This type of variant without explicit consideration of an OR is occasionally referred to as a correspondence variant [51,66] which might also be better called stretch variant [67]. The number of stretch variants would be observed in physical reality if $\mathcal{H} = \mathcal{G}^C = 12\,1$ (considering proper rotations only, see Section 3.1).

Concerning the appearance of the Kikuchi lines in an EBSD pattern, the effect of such a strain has two consequences:

- The isotropic volume change due to the strain will lead to a change of the widths of all Kikuchi bands, which will be hardly visible.
- The deviatoric part of the strain will lead to change in the widths of certain bands and, more importantly for standard EBSD analysis, to a change in the intraband angles.

Hence, it is desirable to decompose $\boldsymbol{\varepsilon}_{\eta \to \eta_{1,2}'}$ into an isotropic part $\frac{1}{3}\mathrm{Tr}\boldsymbol{\varepsilon}_{\eta \to \eta_1'}$ and a deviatoric part $\boldsymbol{\varepsilon}^{\mathrm{dev}}_{\eta \to \eta_{1,2}'}$. This is justified here by the small magnitude of the strains, making an infinite strain treatment sufficient:

$$\boldsymbol{\varepsilon}^{\mathrm{dev}}_{\eta \to \eta_{1,2}'} = \boldsymbol{\varepsilon}_{\eta \to \eta_{1,2}'} - \frac{1}{3}\mathrm{Tr}\boldsymbol{\varepsilon}_{\eta \to \eta_1'} = \begin{pmatrix} 0.00526 & 0 & \mp 0.00399 \\ 0 & 0.00713 & 0 \\ \mp 0.00399 & 0 & -0.01239 \end{pmatrix} \tag{A5}$$

Note that this deviatoric strain differs for non-cubic systems from the Aizu strain [68] used in some previous works to assess metrical distortions (e.g., [69,70]) without reference to a parent state. A latter is available here in form of the η phase. The deviatoric strain $\boldsymbol{\varepsilon}^{\mathrm{dev}}_{\eta \to \eta_1'}$ calculated as a next step, however, basically corresponds to the Aizu strain.

Upon indexing the Kikuchi bands in EBSD patterns in the present case, it is crucial to distinguish between not only an EBSD pattern by the η and by the η'' phase, but also between two orientations of the η' phase approximately differing by the above-mentioned 180° rotation of the η' structure around $\hat{\mathbf{e}}_3$. While the value of $\boldsymbol{\varepsilon}^{\mathrm{dev}}_{\eta \to \eta_{1,2}'}$ is the basis for distinction of η' from η, the basis for distinction of orientations of η' occurs by the difference

of the corresponding two transformations strains (or of their deviatoric parts, the result being the same):

$$\Delta\varepsilon_{\eta_1'\to\eta_2'} = \varepsilon_{\eta\to\eta_2'}^{dev} - \varepsilon_{\eta\to\eta_1'}^{dev} = \begin{pmatrix} 0 & 0 & 0.00797 \\ 0 & 0 & 0 \\ 0.00797 & 0 & 0 \end{pmatrix}. \tag{A6}$$

The deformation implied by $\Delta\varepsilon_{\eta_1'\to\eta_2'}$, of course only describes the changes of the lattices of the substructures, without considering the change in the superstructure. The strain matrices relating the different types of patterns are arranged in Figure A1.

In view of Aizu [68], using the Frobenius norm, i.e., square root of the sum of the squares of the components of the strain tensors, one finds $\|\varepsilon_{\eta\to\eta_1'}^{dev}\|_F = \|\varepsilon_{\eta\to\eta_2'}^{dev}\|_F = 0.018$ and $\|\Delta\varepsilon_{\eta_1'\to\eta_2'}\|_F = 0.011$. It is suggested that distinction between the different states η, η_1' and η_2' in EBSD patterns gets easier if the Frobenius norm of the (deviatoric) strain distinguishing the states increases. In view of the similar values of 0.018 and 0.011, both problems, namely distinguishing η from η' and distinguishing the two principal domain states of η', would occur with similar ease or difficulty. The use of the strain tensor and Frobenius norm as measure for the ease or difficulty in separating phases or orientations based on small metric differences including various examples will be presented in detail in another paper.
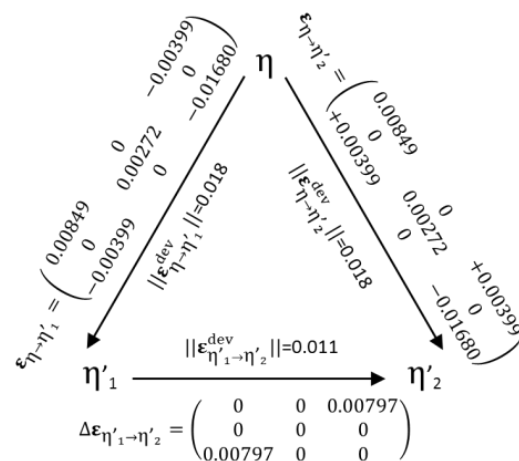

Figure A1. Symmetric strains relating the structures of the orthorhombic η phase and the two principal domain states of the monoclinic η' phase as calculated on the basis of the lattice parameters given in Table 2. The strains are given in the directions of the arrows. The reverse arrow directions imply the corresponding negative strains.

Appendix C. Accuracy of Trace Determination

In the following section, the accuracy with which the indices of the trace can be determined is estimated. The origin of the deviation from the real trace indices can be (1) image distortions, (2) an irregular shape of the variants (e.g., due to deviation from a perfectly planar habit plane) and (3) the measured crystallographic orientation itself. Deviations due to lens errors in electron optics might be neglected in the employed SEMs.

(1) A high sample tilt angle such as the 70° most often applied during EBSD measurements is responsible for geometrically-caused image distortions [53]. Even small deviations of sample surface from parallelism of the plane of the tilted stage cause large rhomboidal distortions which are approx. 3 times larger errors in the projected image than the deviation in the sample set-up [53]. A trapezium distortion must be considered when low magnifications are employed and can be neglected in the present case of applied high magnifications [53]. Using the example of the particle in Figure 2b, the relevance of image distortion is emphasized in Figure A2a. The trace orientation

differs by 6° if measured for the tilted instead of for the untilted state. Therefore, the latter is used for determination of trace orientation via angle α to describe the traces in the sample coordinate system. Additionally, effects of beam or image drift can lead to image distortions (which a very sample- and system-dependent), especially for long acquisition times such as during the EBSD measurements which was only 1.3° of the trace in the EBSD map to the image in the tilted state (Figure A2). Thus, the error can be reduced using images with moderate acquisition times for the measurement of the trace orientation. Consequently, it is highly recommended that the trace orientation should be measured on an untilted BSE or SE image to avoid errors from image distortions. Image distortions also influence relative and absolute crystallographic orientation data. Nevertheless, the relative accuracy between orientations is mainly affected at low magnifications and is largely avoidable using an appropriate projection center calibration from the mapping center to edge [53]. However, for absolute orientations, a misalignment of the sample and stage coordinate systems leads to misinterpretations of the orientation information and is, therefore, reflected in the accuracy of the measured traces. Although it might be recommended to correct the orientations for the misalignment, correct alignment information is hardly accessible. Therefore, present orientation data were not corrected. However, in this study, the sample had been mounted and remounted several times between the measurements of the particles, so that errors from image distortion should be averaged.

(2)   Often habit planes are not detectable as perfectly planar planes in a microstructure. These planes can have curvatures or modulations. Moreover, in the present case of η′ variants within the η matrix, the variants have not straight planar edges but appear with needle- or lens-like shaped variants. However, not all variants are symmetric or similarly curved as neighboring variants. Therefore, a mean central line of the neighboring variants is used to determine the trace orientation (Figure A2b).

(3)   Next to image distortion, different adjustments of indexing parameters also lead to slightly different orientation solutions. Moreover, offsets of the projection center calibration at high magnifications lead to slightly different orientation solutions when comparing the different maps. The misorientation angle is between 0.5° and 1° for the same pixels in different maps in Figure 4, indexed with PCX = 0.547 but PCY = 0.76 or PCY = 0.77. Similarly, e.g., the Hough-space resolution, the choice of band centers and band edges, and number of bands, lead to slightly different orientation solutions.

Finally, considering all the sources impairing the accuracy of a measured trace, one should be aware that the actual traces are at least approx. ±5° off from the measured trace.
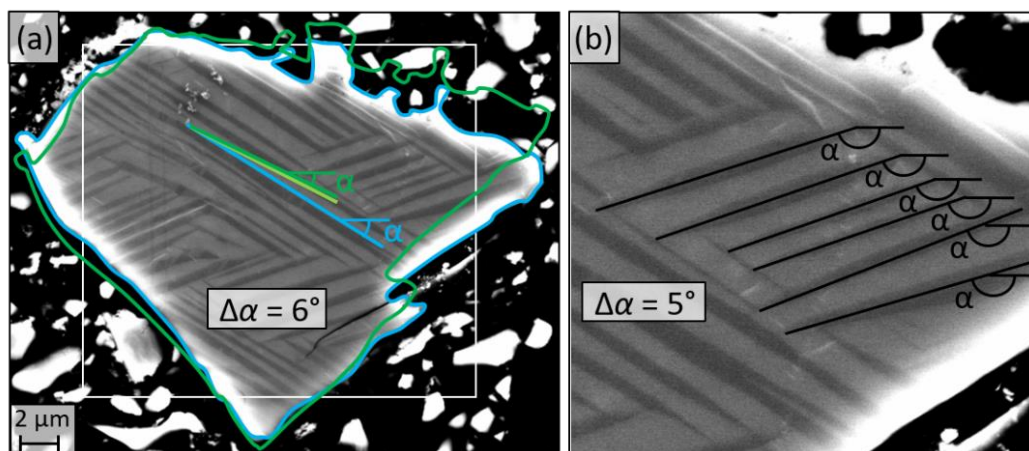

Figure A2. (**a**) Image distortions comparing the contours of the particle imaged in the untilted state (showing BSE contrast, contour line: blue) and the tilted state (contour line: green). (**b**) Spread of measured α angles in neighboring "parallel" bands with tapered ends if angle is measured close to the end.

Appendix D. Effect of Minimization Functional

The minimization functional $\chi^2(\hat{\mathbf{h}}^P)$ in Equations (9a), (11a,b) and (12) has been chosen mainly because least squares fitting is most common. However, the exponent $q = 2$ has been replaced by a more general $q < 2$ and results in habit planes that are more robust with respect to outliers have been minimized. More specifically, minimizing χ^q with $q = 0.1$ for the original, uncorrected child orientations yields the habit plane $\{1\ 1.7\ 2.4\}_{\eta'}$ which is much closer to the eventually found habit plane $\{1\ 1.8\ 2.5\}_{\eta'}$ than the habit plane $\{1\ 4.4\ 5.8\}_{\eta'}$ found by optimizing the traditional functional χ^2.

$$\chi^q(\hat{\mathbf{h}}^P) = \frac{1}{N} \sum_{n=1}^{N} \left(90° - \omega(\hat{\mathbf{r}}^P(n), \hat{\mathbf{h}}^P)\right)^q \rightarrow min \tag{A7}$$

The functionals $\chi^{0.1}$ for the child traces, the parent traces and the variant corrected parent traces are depicted in Figure A3. The thin black lines indicate the great circles perpendicular to the traces. Hence, the optimal habit plane normal is the spot where most of these great circles intersect.

It also becomes evident that a higher symmetry complicates the fitting procedure, as more circles may interfere (Figure A3b,c). Reducing the number of wrongly interfering circles is the key advantage of the variant based trace correction method (Figure A3c).
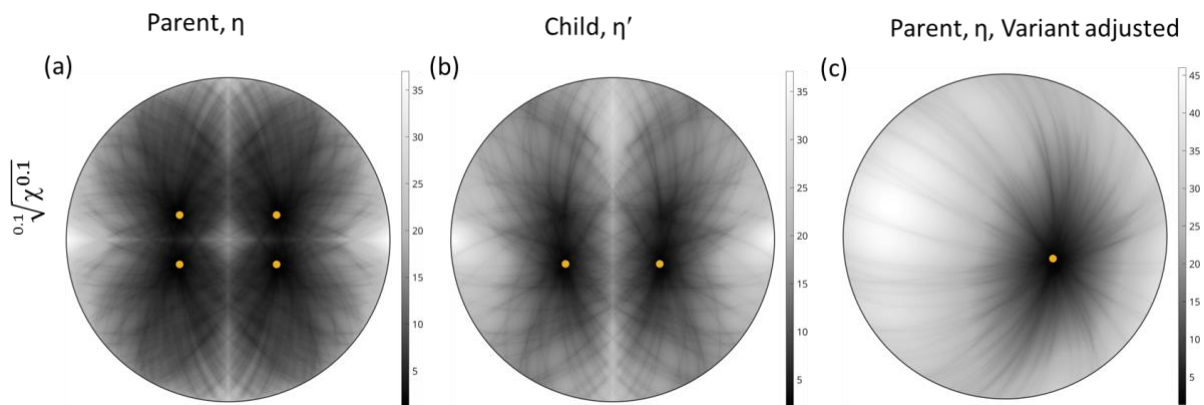

Figure A3. Illustration of the direction-dependent value $\sqrt[0.1]{\chi^{0.1}}$ for uncorrected parent traces (**a**), uncorrected child traces (**b**) and the variant adjusted parent traces (**c**). The orange points indicate the determined habit plane poles at the minimum.

References

1. Denner, S.G.; Jones, R.D. Kinetic interactions between aluminium$_{liquid}$ and iron/steel$_{solid}$ for conditions applicable to hot-dip aluminizing. *Met. Technol.* **1977**, *4*, 167–174. [CrossRef]
2. Kwon, S.C.; Lee, J.Y. Interface Morphology between the Aluminide Layer and Iron Substrate in the Hot-Dip Aluminizing Process. *Can. Metall. Q.* **1981**, *20*, 351–357. [CrossRef]
3. Bahadur, A.; Mohanty, O.N. Structural Studies of Hot Dip Aluminized Coatings on Mild Steel. *Mater. Trans. JIM* **1991**, *32*, 1053–1061. [CrossRef]
4. Bouché, K.; Barbier, F.; Coulet, A. Intermetallic compound layer growth between solid iron and molten aluminium. *Mater. Sci. Eng. A* **1998**, *249*, 167–175. [CrossRef]
5. Kobayashi, S.; Yakou, T. Control of intermetallic compound layers at interface between steel and aluminum by diffusion-treatment. *Mater. Sci. Eng. A* **2002**, *338*, 44–53. [CrossRef]
6. Bouayad, A.; Gerometta, C.; Belkebir, A.; Ambari, A. Kinetic interactions between solid iron and molten aluminium. *Mater. Sci. Eng. A* **2003**, *363*, 53–61. [CrossRef]
7. Jindal, V.; Srivastava, V.C.; Das, A.; Ghosh, R.N. Reactive diffusion in the roll bonded iron–aluminum system. *Mater. Lett.* **2006**, *60*, 1758–1761. [CrossRef]

8.   Kajihara, M. Quantitative Evaluation of Interdiffusion in Fe_2Al_5 during Reactive Diffusion in the Binary Fe–Al System. *Mater. Trans.* **2006**, *47*, 1480–1484. [CrossRef]

9.   Shahverdi, H.R.; Ghomashchi, M.R.; Shabestari, S.; Hejazi, J. Microstructural analysis of interfacial reaction between molten aluminium and solid iron. *J. Mater. Process. Technol.* **2002**, *124*, 345–352. [CrossRef]

10.   Sasaki, T.; Yakou, T. Features of intermetallic compounds in aluminized steels formed using aluminum foil. *Surf. Coat. Technol.* **2006**, *201*, 2131–2139. [CrossRef]

11.   Tanaka, Y.; Kajihara, M. Morphology of Compounds Formed by Isothermal Reactive Diffusion between Solid Fe and Liquid Al. *Mater. Trans.* **2009**, *50*, 2212–2220. [CrossRef]

12.   Cheng, W.-J.; Wang, C.-J. Growth of intermetallic layer in the aluminide mild steel during hot-dipping. *Surf. Coat. Technol.* **2009**, *204*, 824–828. [CrossRef]

13.   Cheng, W.-J.; Wang, C.-J. Study of microstructure and phase evolution of hot-dipped aluminide mild steel during high-temperature diffusion using electron backscatter diffraction. *Appl. Surf. Sci.* **2011**, *257*, 4663–4668. [CrossRef]

14.   Cheng, W.-J.; Wang, C.-J. Effect of silicon on the formation of intermetallic phases in aluminide coating on mild steel. *Intermetallics* **2011**, *19*, 1455–1460. [CrossRef]

15.   Watanabe, M.; Feng, K.; Nakamura, Y.; Kumai, S. Growth Manner of Intermetallic Compound Layer Produced at Welding Interface of Friction Stir Spot Welded Aluminum/Steel Lap Joint. *Mater. Trans.* **2011**, *52*, 953–959. [CrossRef]

16.   Takata, N.; Nishimoto, M.; Kobayashi, S.; Takeyama, M. Morphology and formation of Fe–Al intermetallic layers on iron hot-dipped in Al–Mg–Si alloy melt. *Intermetallics* **2014**, *54*, 136–142. [CrossRef]

17.   Becker, H.; Heger, D.; Leineweber, A.; Rafaja, D. Modification of the Diffusion Process in the Iron-Aluminum System via Spark Plasma Sintering/Field Assisted Sintering Technology. *Defect Diffus. Forum* **2016**, *367*, 1–9. [CrossRef]

18.   Chen, S.; Yang, D.; Zhang, M.; Huang, J.; Zhao, X. Interaction between the Growth and Dissolution of Intermetallic Compounds in the Interfacial Reaction between Solid Iron and Liquid Aluminum. *Metall. Mater. Trans. A* **2016**, *47*, 5088–5100. [CrossRef]

19.   Richards, R.W.; Jones, R.D.; Clements, P.D.; Clarke, H. Metallurgy of continuous hot dip aluminizing. *Intern. Mater. Rev.* **1994**, *39*, 191–212. [CrossRef]

20.   Sakiyama, T.; Naito, Y.; Miyazaki, Y.; Nose, T.; Gurayama, G.; Saita, K.; Oikawa, H. Dissimilar Metal Joining Technologies for Steel Sheet and Aluminum Alloy Sheet in Auto Body. *Nippon Steel Tech. Rep.* **2013**, *103*, 91–98.

21.   Naoi, D.; Kajihara, M. Growth behavior of Fe_2Al_5 during reactive diffusion between Fe and Al at solid-state temperatures. *Mater. Sci. Eng. A* **2007**, *459*, 375–382. [CrossRef]

22.   Maki, J.; Suehiro, M.; Ikematsu, Y. Alloying Reaction of Aluminized Steel Sheet. *ISIJ Int.* **2010**, *50*, 1205–1210. [CrossRef]

23.   Springer, H.; Kostka, A.; dos Santos, J.F.; Raabe, D. Influence of intermetallic phases and Kirkendall-porosity on the mechanical properties of joints between steel and aluminium alloys. *Mater. Sci. Eng. A* **2011**, *528*, 4630–4642. [CrossRef]

24.   Becker, H.; Amirkhanyan, L.; Kortus, J.; Leineweber, A. Powder-X-ray diffraction analysis of the crystal structure of the η′-Al_8Fe_3 (η′-$Al_{2.67}$Fe) phase. *J. Alloys Compd.* **2017**, *721*, 691–696. [CrossRef]

25.   Han, K.; Ohnuma, I.; Kainuma, R. Experimental determination of phase equilibria of Al-rich portion in the Al–Fe binary system. *J. Alloys Compd.* **2016**, *668*, 97–106. [CrossRef]

26.   Li, X.; Scherf, A.; Heilmaier, M.; Stein, F. The Al-Rich Part of the Fe-Al Phase Diagram. *J. Phase Equilibria Diffus.* **2016**, *37*, 162–173. [CrossRef]

27.   Hamada, T.; Higashi, M.; Niitsu, K.; Inui, H. Phase equilibria among η-Fe_2Al_5 and its higher-ordered phases. *Sci. Technol. Adv. Mater.* **2021**, *22*, 373–385. [CrossRef]

28.   Becker, H.; Zienert, T.; Wetzel, M.; Leineweber, A. Ordering Strains in Al_5Fe_2. In Proceedings of the 15th European Powder Diffraction Conference, Bari, Italy, 12–15 June 2016. [CrossRef]

29.   Okamoto, N.L.; Okumura, J.; Higashi, M.; Inui, H. Crystal structure of η′-Fe_3Al_8; low-temperature phase of η-Fe_2Al_5 accompanied by an ordered arrangement of Al atoms of full occupancy in the c-axis chain sites. *Acta Mater.* **2017**, *129*, 290–299. [CrossRef]

30.   Becker, H.; Leineweber, A. Atomic channel occupation in disordered η-Al_5Fe_2 and in two of its low-temperatures phases, η″ and η‴. *Intermetallics* **2018**, *93*, 251–262. [CrossRef]

31.   Okamoto, N.L.; Higashi, M.; Inui, H. Crystal structure of η″-Fe_3Al_{7+x} determined by single-crystal synchrotron X-ray diffraction combined with scanning transmission electron microscopy. *Sci. Technol. Adv. Mater.* **2019**, *20*, 543–556. [CrossRef]

32.   Takata, N.; Nishimoto, M.; Kobayashi, S.; Takeyama, M. Crystallography of Fe_2Al_5 phase at the interface between solid Fe and liquid Al. *Intermetallics* **2015**, *67*, 1–11. [CrossRef]

33.   Burkhardt, U.; Grin, Y.; Ellner, M.; Peters, K. Structure refinement of the iron–aluminium phase with the approximate composition Fe_2Al_5. *Acta Crystallogr. B* **1994**, *50*, 313–316. [CrossRef]

34.   Oxford Instruments. *HKL Channel 5, A/S June 2007 User Manual*; Oxford Instruments: Hobro, Denmark, 2007.

35.   Bachmann, F.; Hielscher, R.; Schaeben, H. Grain detection from 2d and 3d EBSD data—Specification of the MTEX algorithm. *Ultramicroscopy* **2011**, *111*, 1720–1733. [CrossRef] [PubMed]

36.   Bachmann, F.; Hielscher, R.; Schaeben, H. Texture Analysis with MTEX—Free and Open Source Software Toolbox. *Sol. State Phen.* **2010**, *160*, 63–68. [CrossRef]

37. Wondratschek, H.; Jeitschko, W. Twin domains and antiphase domains. *Acta Crystallogr. A* **1976**, *32*, 664–666. [CrossRef]
38. Cayron, C. Groupoid of orientational variants. *Acta Crystallogr. A* **2006**, *62*, 21–40. [CrossRef]
39. van Tendeloo, G.; Amelinckx, S. Group-theoretical considerations concerning domain formation in ordered alloys. *Acta Crystallogr. A* **1974**, *30*, 431–440. [CrossRef]
40. Cahn, J.W.; Kalonji, G. Symmetry in Solid State Transformation Morphologies. *Proc. Int. Conf. Solid-Solid Phase Transform.* **1981**, 3–14.
41. Tolédano, P.; Dmitriev, V. Reconstructive phase transitions. In *Crystals and Quasicrystals*; Word Scientific: Singapore, 1996; ISBN 978-981-02-2364-9.
42. Krakow, R.; Bennett, R.J.; Johnstone, D.N.; Vukmanovic, Z.; Solano-Alvarez, W.; Lainé, S.J.; Einsle, J.F.; Midgley, P.A.; Rae, C.M.F.; Hielscher, R. On three-dimensional misorientation spaces. *Proc. Math. Phys. Eng. Sci.* **2017**, *473*, 20170274. [CrossRef]
43. Torrès, J.; Roucau, C.; Ayroles, R. Investigation of the interactions between ferroelastic domain walls and the structural transition in lead phosphate observed by electron microscopy: I. Experimental results. *Phys. Status Solidi (A)* **1982**, *70*, 659–669. [CrossRef]
44. Torrès, J.; Roucau, C.; Ayeoles, R. Investigation of the interactions between ferroelastic domain walls and of the structural transition in lead phosphate observed by electron microscopy. II. Interpretation of the interactions between ferroelastic domain walls. *Phys. Status Solidi (A)* **1982**, *71*, 193–205. [CrossRef]
45. Salje, E.K.H. *Phase Transitions in Ferroelastic and Co-Elastic Crystals: An Introduction for Mineralogists, Material Scientists and Physicists*; Cambridge University Press: Cambridge, CA, USA, 1990; ISBN 9780521384490.
46. Zhang, M.-X.; Kelly, P.M. Crystallographic features of phase transformations in solids. *Prog. Mater. Sci.* **2009**, *54*, 1101–1170. [CrossRef]
47. Nolze, G.; Jürgens, M.; Olbricht, J.; Winkelmann, A. Improving the precision of orientation measurements from technical materials via EBSD pattern matching. *Acta Mater.* **2018**, *159*, 408–415. [CrossRef]
48. Nolze, G.; Winkelmann, A.; Neumann, R.S. Significant Improvement of the orientation resolution by EBSD-pattern matching. In Proceedings of the Talk at the German EBSD Meeting, Geesthacht, Germany, 7–11 May 2017.
49. Bachmann, F.; Hielscher, R.; Jupp, P.E.; Pantleon, W.; Schaeben, H.; Wegert, E. Inferential statistics of electron backscatter diffraction data from within individual crystalline grains. *J. Appl. Crystallogr.* **2010**, *43*, 1338–1355. [CrossRef]
50. Zhang, W.-Z.; Weatherly, G.C. On the crystallography of precipitation. *Prog. Mater. Sci.* **2005**, *50*, 181–292. [CrossRef]
51. Bhattacharya, K. *Microstructure of Martensite: Why it Forms and How It Gives Rise to the Shape-Memory Effect*; Oxford University Press: Oxford, UK, 2007; ISBN 0198509340.
52. Hirose, S.; Itoh, T.; Makita, M.; Fujii, S.; Arai, S.; Sasaki, K.; Saka, H. Defect structure of deformed Fe_2Al_5 intermetallic compound. *Intermetallics* **2003**, *11*, 633–642. [CrossRef]
53. Nolze, G. Image distortions in SEM and their influences on EBSD measurements. *Ultramicroscopy* **2007**, *107*, 172–183. [CrossRef]
54. Rowlands, P.C.; Fearon, E.O.; Bevis, M. Deformation Twinning in Fe-Ni and Fe-Ni-C Martensites. *Trans. Met. Soc. AIME* **1968**, *242*, 1559–1562.
55. Wang, Z.; Zaefferer, S. On the accuracy of grain boundary character determination by pseudo-3D EBSD. *Mater. Charact.* **2017**, *130*, 33–38. [CrossRef]
56. Randle, V. Crystallographic characterization of planes in the scanning electron microscope. *Mater. Charact.* **1995**, *34*, 29–34. [CrossRef]
57. Schumann, H.; Richter, G.; Leineweber, A. Crystallography of a-Fe whiskers. *J. Appl. Crystallogr.* **2020**, *53*, 865–879. [CrossRef] [PubMed]
58. Zaefferer, S.; Wright, S.I.; Raabe, D. Three-Dimensional Orientation Microscopy in a Focused Ion Beam–Scanning Electron Microscope: A New Dimension of Microstructure Characterization. *Metall. Mater. Trans. A* **2008**, *39*, 374–389. [CrossRef]
59. Dash, M.K.; Karthikeyan, T.; Saroja, S. Five-Parameter Grain Boundary Determination in Annealed Ferrite Structure Using Electron Backscatter Diffraction and Serial Sectioning Technique. *Trans. Ind. Inst. Met.* **2017**, *70*, 133–143. [CrossRef]
60. Schumann, H.; Leineweber, A. Crystallography of γ'-Fe_4N formation on bulk polycrystalline α-Fe substrates. *Materialia* **2021**, *17*, 101119. [CrossRef]
61. Randle, V. Application of EBSD to the analysis of interface planes: Evolution over the last two decades. *J. Microsc.* **2008**, *230*, 406–413. [CrossRef]
62. Saylor, D.M.; El-Dasher, B.S.; Adams, B.L.; Rohrer, G.S. Measuring the five-parameter grain-boundary distribution from observations of planar sections. *Metall. Mater. Trans. A* **2004**, *35*, 1981–1989. [CrossRef]
63. Becker, H.; Leineweber, A. Approximate icosahedral symmetry of α-Al(Fe,Mn,Cr)Si in electron backscatter diffraction analysis of a secondary Al-Si casting alloy. *Mater. Charact.* **2018**, *141*, 406–411. [CrossRef]
64. Giacovazzo, C. (Ed.) *Fundamentals of Crystallography*, 3rd ed.; Oxford University Press: Oxford, UK, 2011; ISBN 9780199573653.
65. Chen, X.; Song, Y.; Tamura, N.; James, R.D. Determination of the stretch tensor for structural transformations. *J. Mech. Phys. Solids* **2016**, *93*, 34–43. [CrossRef]
66. Gao, Y.; Shi, R.; Nie, J.-F.; Dregia, S.A.; Wang, Y. Group theory description of transformation pathway degeneracy in structural phase transformations. *Acta Mater.* **2016**, *109*, 353–363. [CrossRef]
67. Cayron, C. The transformation matrices (distortion, orientation, correspondence), their continuous forms and their variants. *Acta Crystallogr. A* **2019**, *75*, 411–437. [CrossRef] [PubMed]

68. Aizu, K. Determination of the State Parameters and Formulation of Spontaneous Strain for Ferroelastics. *J. Phys. Soc. Jpn.* **1970**, *28*, 706–716. [CrossRef]

69. Wieser, C.; Walnsch, A.; Hügel, W.; Leineweber, A. The monoclinic lattice distortion of η′-Cu_6Sn_5. *J. Alloys Compd.* **2019**, *794*, 491–500. [CrossRef]

70. Leineweber, A.; Kriegel, M.J.; Distl, B.; Martin, S.; Klemm, V.; Shang, S.-L.; Liu, Z.-K. An orthorhombic $D0_{22}$-like precursor to Al_8Mo_3 in the Al–Mo–Ti system. *J. Alloys Compd.* **2020**, *823*, 153807. [CrossRef]